Journal of Sound and Vibration (2001) **240**(5), 859–889
doi:10.1006/jsvi.2000.3264, available online at http://www.idealibrary.com on IDEAL®

PROPER ORTHOGONAL DECOMPOSITION (POD) OF A CLASS OF VIBROIMPACT OSCILLATIONS

M. F. A. AZEEZ† AND A. F. VAKAKIS

Department of Mechanical and Industrial Engineering, University of Illinois at Urbana Champaign, Urbana, Illinois-61801, *U.S.A.*

(*Received* 4 *September* 1998, *and in final form* 31 *July* 2000)

This study employs the method of proper orthogonal decomposition (POD), also known as the Karhunen–Loeve (K–L) method, to extract dominant coherent structures (modes that approximate the system behavior) from time-series data. These mode shapes can be used in a Galerkin reconstruction process to obtain lower dimensional models for the structural systems under consideration. The mode shapes and the energies obtained by this process can also be used to predict certain kinds of periodic or non-periodic non-linear motions. The K–L method has been applied successfully to fluid dynamical, thermal processes and signal processing. However, only a handful of works exist in the area of vibration analysis and structural mechanics. An extensive K–L analysis is performed numerically for two vibroimpacting systems: a beam and a rotor. Lower dimensional models are created and used to study non-linear energy transmission from low to higher K–L modes. Extensive reconstructions are also performed to prove the efficacy of the K–L method to provide accurate low-dimensional dynamical models. In addition, experimental investigations are presented for the case of the overhung impacting rotor and qualitative comparisons with the theoretical analysis are presented.

1. INTRODUCTION

The method of proper orthogonal decomposition (POD) or Karhunen–Loeve (K–L) decomposition is a means of extracting spatial information from a set of time-series data available on a domain. In acoustical and random signal decomposition, the Karhunen–Loeve decomposition method (also known as proper orthogonal decomposition) has been widely used to ascertain the modes and the energy of the signals under consideration [1, 2]. This is very important in applications that involve compression and storage of stochastic signals. The use of Karhunen–Loeve (K–L) transform [3] is of great value in non-linear settings where traditional linear techniques such as modal testing and power spectrum analyses cannot be applied. This is especially the case for non-linear engineering structures. The Karhunen–Loeve decomposition can be used to obtain low-dimensional dynamic models of distributed parameter systems, by computing orthogonal eigenfunctions by post-processing experimental or numerical data of the system response. These eigenfunctions are optimal in the sense that fewer K–L modes are needed to account for the same amount of vibrational energy, compared to modes resulting from application of standard Galerkin or Rayleigh–Ritz procedures [4]. This technique can

†Currently member of staff at General Electric Corporate R&D Center.

0022-460X/01/100859 + 31 $35.00/0

conveniently treat non-linear distributed parameter systems defined on irregular domains to yield discretized systems with only a few degrees of freedom, which can then be used to reconstruct the dynamical response.

The Karhunen–Loeve analysis has additional distinctive advantages. The modes obtained from the K–L decomposition for a certain set of system parameters can, in most cases, be used to reconstruct the response of a system whose parameters are slightly different from the original system. The modes would atleast serve as an orthogonal basis in the absence of a better basis. In the area of vibrations of structures, the Karhunen–Loeve modes can be used to solve the non-linear governing equations accurately. This method has been used successfully in the field of fluid dynamics [5–7]. The key advantage of this method lies in the fact that it can be applied, not only to Hamiltonian systems, but also to dissipative ones, and provides information about the spatial structure of the dynamics as well as the energy contained in them. Hence, this method could be a valuable tool in the analysis and system identification of the dynamics of engineering structures.

Few works exist, to date, on the application of the K–L method to engineering dynamics. The K–L method was primarily introduced as a means of extracting dominant energy signals from a stochastic random process [8, 9]. Since then, the application of this method in fluid dynamics, thermal problems and signal processing has been extensive. In reference [10] the method has been applied to a turbulent thermal convective system and low-order models were created to study the dynamics of the thermal behavior. In reference [11] the modes of a reaction–diffusion chemical process are captured by means of the K–L method and the dynamical behavior is ascertained. The snapshot method is used by Rajaee *et al.* [6] to describe the dynamics of the coherent structure of a weakly perturbed free shear layer. Sirovich and Kirby [7] use the K–L method of snapshots to capture the dynamical structure of a two-dimensional axisymmetric jet. Sirovich employs the K–L method in different fluid dynamical contexts as reported in references [7, 12, 4, 5]. In reference [13] Park and Cho examine the efficacy of the K–L method for the control of distributed parameter systems. The notable works in structural mechanics are those by Mari and Cusumano [14, 15]. In the latter the dimensionality of the dynamics of an impacting beam is studied by means of traditional time-delay techniques and K–L decomposition. The energy transfer between K–L modes is also studied experimentally, in that work. In reference [16] K–L decomposition was used to perform system identification of an aeroelastic problem.

In this work, the K–L method is applied to continuous systems with infinite degrees of freedom that undergo vibroimpacts; specifically, vibroimpacting beams and overhung rotors are considered. The mathematical preliminaries are briefly presented and the Method of Snapshots is also described. The method is then applied to an impacting beam system, where the modes are extracted and energy transfer patterns are noted. The identified K–L modes are then used to create low-dimensional models, via a Galerkin projection. The method is also applied to an overhung rotor undergoing vibroimpacts. The chief aims of the paper are: (a) to study the non-linear effects of vibroimpacts on the dynamics; (b) to investigate energy transfer patterns from low- to high-order K–L modes due to the vibroimpacts; (c) to show how the K–L modes can lead to accurate low-dimensional models for the dynamics; and (d) to demonstrate that the K–L method can provide a useful and powerful tool to identify real-time structural variations in the system such as the ones caused by defects. Hence, a goal of this work is to show that based on K–L decomposition one can develop monitoring and diagnostic tools for complex rotordynamic systems. Finally, an experimental study is performed on a vibroimpacting overhung rotor.

2. THEORY OF K–L DECOMPOSITION

The K–L decomposition, in essence, is a method of representing a stochastic system in terms of a minimum number of degrees of freedom. The system under investigation is deterministic in the sense that, for a given set of inputs, the output is always the same without any uncertainty. This is done by processing experimental or numerical data obtained at measurement stations distributed throughout the system. The definitions and formulation steps can be found in many references [12, 4, 3], but the definitions here follow closely the ones used in reference [13]. Define a random field $u(x, t)$ on some domain Ω. In general, this field can be vector valued, but only scalar-valued functions are considered here for convenience. This field is first decomposed into mean ($U(x) = \langle u \rangle$) and time-varying ($v(x, t)$) parts. This is represented as

$$u(x, t) = U(x) + v(x, t). \tag{1}$$

In any practical situation (both experimental and numerical), the fields $u(x, t)$ and $v(x, t)$ are available at a finite number of points in space and time. Hence at a given time t_n, when we look at the system, the system displays a *snapshot* v_n; the collection or ensemble of snapshots is represented by $\{v_n\}$. At this stage it is assumed that the snapshot $\{v_n(x)\}$ is a continuous function of x, where $x \in \Omega$. The problem now is to obtain the most typical or characteristic structure $\phi(x)$ among these snapshots $\{v_n\}$. This is done by minimizing the objective function λ as follows:

$$\text{Minimize} \left\{ \bar{\lambda} = \sum_{n=1}^{N} (\phi(x) - v_n(x))^2 \right\} \quad \forall x \in \Omega, \tag{2}$$

where there are N snapshots of the random field, on the domain Ω. The above minimization is carried out pointwise for each x. Equation (2) can be posed as an eigenvalue problem. Hence, several solutions to $\phi(x)$ can exist. In order to make the computation unique, the following normality condition is imposed:

$$\int_{\Omega} \phi(x)^2 \, \mathrm{d}x = 1, \tag{3}$$

and to simplify the derivations, the following notations are employed:

$$v(x, t), \quad \text{a random field defined in } \Omega, \text{ the function space;} \tag{4}$$

$$\{v_n\}, \quad \text{a collection of snapshots of } v(x); \tag{5}$$

$$(f, g) \equiv \int_{\Omega} f(x) g(x) \, \mathrm{d}\Omega, \quad \text{inner product of two functions in } \Omega; \tag{6}$$

$$\langle v_n \rangle \equiv \frac{1}{N} \sum_{n=1}^{N} v_n(x), \quad \text{average of snapshots.} \tag{7}$$

Equation (2) means that the sum of the differences squared between $v_n(x)$ and $\phi(x)$ should be minimized. In other words, the ensemble average of the inner products between v_n and ϕ must be maximized. By using the above notations and expanding equation (2) while utilizing equation (3) the problem reduces to the maximization of $\langle (\phi, v_n) \rangle$. We also need

$\langle(\phi, v_n)\rangle$ to be positive (to move closer to a true minimum) and hence we maximize $\langle(\phi, v_n)^2\rangle$. Equation (2) can now be posed in a compact form as

$$\text{Maximize} \left\{\lambda = \frac{\langle(\phi, v_n)^2\rangle}{(\phi, \phi)}\right\} \quad \text{w.r.t. } \phi(x). \tag{8}$$

The numerator of the right-hand side of this equation is now expanded using the notation for the inner product o yield

$$\langle(\phi, v_n)^2\rangle = \left\langle \int_\Omega \phi(x) v_n(x)\,\mathrm{d}x \int_\Omega \phi(x') v_n(x')\,\mathrm{d}x' \right\rangle \tag{9}$$

$$= \int_\Omega \left\{ \int_\Omega \langle v_n(x) v_n(x')\rangle \phi(x)\,\mathrm{d}x \right\} \phi(x')\,\mathrm{d}x'. \tag{10}$$

We now introduce the two-point correlation function (K) defined as

$$K(x, x') = \langle v_n(x) v_n(x')\rangle \equiv \frac{1}{N} \sum_{n=1}^{N} v_n(x) v_n(x') \tag{11}$$

and the linear operator R:

$$R(\,) \equiv \int_\Omega K(x, x')(\,\cdot\,)\,\mathrm{d}x'. \tag{12}$$

Hence, we can represent equation (10) compactly as

$$\langle(\phi, v_n)^2\rangle = \int_\Omega \{R\phi\}\{\phi\}\,\mathrm{d}x = (R\phi, \phi). \tag{13}$$

Inspection of equations (8) and (13) immediately reveals that the optimization problem is reduced to the following integral eigenvalue problem:

$$R\phi = \lambda\phi \Rightarrow \int_\Omega K(x, x')\phi(x')\,\mathrm{d}x' = \lambda\phi(x). \tag{14}$$

This equation has to be solved accurately. There are two ways to solve the problem—the Direct Method and the Method of Snapshots. The choice of the method depends on the nature of the problem. If the function v_n is vector valued and has a smooth transient response, the method of snapshots is preferable [16]. However, if v_n is scalar and the transient response is oscillatory the direct method is more suitable. In the problem considered here the direct method is 20 times faster than the snapshot method. The two methods have been used and compared in reference [17]. The snapshot method alone is presented here. The direct method attempts to solve equation (14) directly using standard numerical schemes and hence the name.

2.1. THE METHOD OF SNAPSHOTS

The solution technique for the method of snapshots is based on the technique used by Sirovich [7]. Here the eigenfunction $\phi(x)$ is assumed to be a linear combination of

snapshots:

$$\phi(x) = \sum_k \alpha_k v_k(x). \tag{15}$$

Substituting equation (15) into equation (14) yields

$$\sum_n \int_\Omega \frac{1}{N} v_n(x) v_n^{\mathrm{T}}(x') \sum_k \alpha_k v_k(x')\,\mathrm{d}x' = \lambda \sum_n \alpha_n v_n(x). \tag{16}$$

This equation yields the following matrix eigenvalue problem:

$$\sum_{k=1}^{N} C_{nk}\alpha_k = \lambda\alpha_n \quad \text{for } n = 1, 2, \ldots, N, \tag{17}$$

$$\Rightarrow [C]\{\alpha\} = \lambda\{\alpha\}, \quad \text{where } C_{nk} = \frac{1}{N}\int_\Omega v_n(x) v_k(x')\,\mathrm{d}x'.$$

The matrix $[C]$ has a dimension $(N \times N)$ and is symmetric and positive definite and $\{\alpha\}$ is a vector of length N containing unknown coefficients α_k. The eigenvalue problem of equation (17) can be conveniently solved to yield real-valued eigenvalues (λ) and eigenvectors (α). It should be noted that the eigenvalues give the strength of the participation of the corresponding eigenfunctions. These eigenvalues should not be interpreted as the real mechanical energy associated with the corresponding mode, but only as the energy of the signal that contains this mode.

The computed eigenvectors (α_n) are then substituted into equation (15), and the eigenfunctions $\phi_n(x)$ are obtained by interpolation. In a practical situation, the snapshots $v_n(x)$ are available at discrete measurement points x_i where $i = 1, \ldots, M$. They can be approximated by cubic splines to create snapshots continuous in $x(v_n(x))$ to be used in the computation of the entries of matrix $[C]$ (equation (17) and the continuous K–L mode shapes $\phi_n(x)$ (equation (16)). Hence, one obtains N eigenfunctions ($\phi_n(x)$) and eigenvalues (λ_n). Suppose that the eigenvalues are ordered such that $\lambda_1 > \lambda_2 > \cdots > \lambda_N$: then the corresponding eigenfunctions represent the most typical structure of the field in the spatial domain Ω. The p-dominant eigenfunctions also known as the K–L modes are obtained as

$$\frac{\sum_{i=1}^{p} \lambda_i}{\sum_{i=1}^{N} \lambda_i} \geqslant 0{\cdot}999 \tag{18}$$

for the smallest integer p. This value of p is also useful to estimate the dimensionality of the system under consideration. Since the kernel ($K(x, x')$) of equation (14) is symmetric, the eigenfunctions satisfy the first order orthogonality condition given by

$$\int_\Omega \phi_i(x)\phi_j(x)\,\mathrm{d}x = 0 \quad \text{if } i \neq j. \tag{19}$$

This orthogonality relation can be used effectively to partially decouple the time and space dependence in the governing partial differential equation. This is discussed in the section where reconstruction of non-linear responses is performed. In equations (12) and (17), the field $\{v_n\}$ is defined on a continuous range of x values on the domain Ω. But in

practice, this field is obtained from experiments or numerical simulations. In these cases, the fields are only available on a discrete set of points in the domain. Hence, smooth interpolations have to be performed to evaluate the integrals accurately. It is imperative that these integrals be very accurately evaluated as even small numerical errors at this stage would render the reconstruction process inaccurate. A high order Gauss Quadrature scheme can compute these integrals very accurately. It should also be noted that the order of the matrix $[C]$ is N: hence if the problem needs several snapshots to be computed then the method of snapshots will be very time consuming. In most situations, the number of dominant modes is much less than N, and hence, not all eigenfunctions need to be computed. The first m eigenvalues and eigenvectors can be effectively computed by means of the IMSL subroutine DEVESF. This can help to reduce computational time to a great extent.

3. CLAMPED BEAM WITH NON-LINEAR SPRINGS

To demonstrate the application of the K–L method, we consider the system shown in Figure 1. It consists of a clamped beam excited close to its clamped end by a harmonic force. Rigid barriers are used to induce symmetrical vibroimpacts close to the free end. The parameters of the system are shown in Table 1. These parameters are the same as those of the beam used to experimentally study localization in a coupled system in a previous work [18]. The flexural rigidity is EI, the linear mass density m and the length is L. The natural frequencies (ω_i) and the modal damping values (d_i), of the cantilever beam without the non-linearity, were obtained experimentally, in reference [18]. The damping values (d_i), given in Table 1, will be used for all the simulations. At $x = a$ vibroimpacts occur, leading

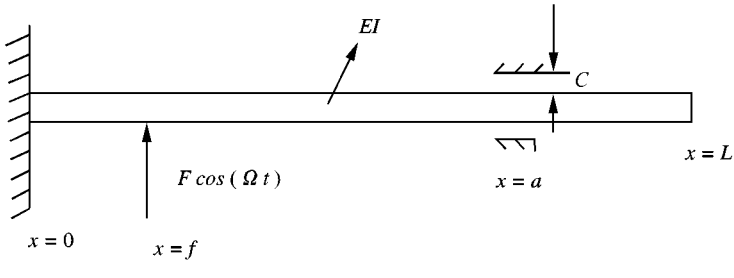

Figure 1. Schematic of the vibroimpacting beam.

TABLE 1

The material and modal parameters of the cantilever beam shown in Figure 1

$EI = 57{\cdot}7028\ \mathrm{Nm}^2$	$m = 0{\cdot}753\ \mathrm{kg/m}$
$L = 0{\cdot}766\ \mathrm{m}$	$a = 0{\cdot}5\ \mathrm{m}$
$\omega_1 = 52{\cdot}455\ \mathrm{rad/s}$	$\omega_2 = 328{\cdot}73\ \mathrm{rad/s}$
$\omega_3 = 920{\cdot}45\ \mathrm{rad/s}$	$\omega_4 = 1803{\cdot}7\ \mathrm{rad/s}$
$\omega_5 = 2981{\cdot}6\ \mathrm{rad/s}$	$\omega_6 = 4454{\cdot}1\ \mathrm{rad/s}$
$d_1 = 0{\cdot}475\ \mathrm{Ns}^2/\mathrm{m}^2$	$d_2 = 0{\cdot}750\ \mathrm{Ns}^2/\mathrm{m}^2$
$d_3 = 0{\cdot}375\ \mathrm{Ns}^2/\mathrm{m}^2$	$d_4 = 0{\cdot}375\ \mathrm{Ns}^2/\mathrm{m}^2$
$d_5 = 0{\cdot}375\ \mathrm{Ns}^2/\mathrm{m}^2$	$d_6 = 0{\cdot}375\ \mathrm{Ns}^2/\mathrm{m}^2$

to strong non-linearities. However, other kinds of smoother non-linearities (cubic, quintic) are also used in some of the following simulations. The displacements at $N_{loc} = 62$ points along the span of the beam are computed by using the assumed modes method where six modes of the cantilever beam are used to partially decouple the governing PDEs, i.e., decouple the second derivative terms w.r.t. time. These displacements are then used to compute the K–L modes. The important factors that affect the K–L computations are the number of snapshots and the spacing between them. A brute force convergence study has to be performed to determine the optimal values of these quantities. The details of this convergence study are reported in reference [17].

3.1. BEAM UNDERGOING VIBROIMPACTS

It is of importance to study how the K–L modes change and the energy transfer between them is affected when various parameters of the system are changed. This can find application in the diagnosis of defects structural systems. Indeed, by computing the K–L modes in real-time and observing the energy transfer from lower to higher K–L modes, one is above to diagnose real-time defects developing in a mechanical system; moreover, one can quantify the effects of these defects on the dynamic response. Hence, the K–L procedure can be an effective *non-parametric* system identification tool that can be used for diagnosis and monitoring in practical mechanical systems. In addition, the relative simplicity of the K–L method enables its application to a wide range of mechanical systems.

In this section, the impacting cantilever beam of Figure 1 is considered for numerical simulations. For the sake of simplicity, two sets of simulations are performed in which the forcing frequency (Ω), location of the forcing (f), and the clearance (c) are changed over a range of values. For each set of simulations f is fixed and the clearance and forcing frequencies are varied. The parameters for the three different simulations (termed henceforth as Sets I and II, for simplicity) are presented in Tables 2 and 3. For each *Case* of each *Set*, the forcing frequency is changed in the order shown in Table 4. The time traces for the snapshots are obtained, as mentioned earlier, by integrating the governing partial differential equations. The simulations are first run for 20 s to eliminate transient responses and then the data are acquired and stored for the computation of the K–L modes.

TABLE 2

Set I: for $f = 0{\cdot}1$ m and $p = 500$ Nt, the clearance (c) is changed as shown

Case no.	1	2	3	4	5	6	7	8	9	10	11	12	13
c (mm)	0	1	2	3	4	5	6	7	8	9	10	20	1000

TABLE 3

Set II: for $f = 0{\cdot}4$ m and $p = 500$ N, the clearance (c) is changed as shown

Case no.	1	2	3	4	5	6	7	8	9	10	11	12	13	14
c (mm)	0	1	2	3	4	6	8	9	10	12	15	20	30	40

TABLE 4

The different forcing frequencies (Ω) of the beam used in the simulations of Sets I and II

Frequency index	1	2	3	4	5	6	7	8	9	10
Ω (rad/s)	30	35	40	45	50	52·4	55	70	80	90
Frequency index	11	12	13	14	15	16	17	18	19	20
Ω (rad/s)	100	110	120	130	140	150	160	170	180	190

3.2. K–L MODE SHAPES

The first and second K–L mode shapes of Set I, Cases 1–6, are presented in Figures 2 and 3. Consider the simulation Set I, Case II, corresponding to a clamped beam without impacts. The K–L mode shape (Figure 2(f)) for frequency indices greater than 13 resembles the second physical mode shape of the cantilever beam. In a linear undamped setting, the K–L modes are nearly identical to the physical modes of the system [19]. Moreover, it can be seen that the energy of the first K–L mode (Figure 5(b)) is essentially equal to the energy of the displacement signals. This is expected as the system is damped and in steady state: hence, the modal contributions of the higher modes are attenuated because the system is excited closer to the first natural frequency. If the system were excited close to its second natural frequency the dominant (first) K–L mode would correspond to the second physical mode of the system. If the system were not damped, there would be considerable contributions from higher modes, depending on the initial conditions of the simulations. However, the systems that occur in nature are always damped. One advantage of the K–L modes is immediately evident: considering an undamped linear beam, if the forcing lies on the node of the second physical mode, the K–L mode does not extract the second mode. In the context of control theory, the second mode is uncontrollable [20] and recourses should be taken to change the control strategy if it is based on the state of the second mode. In this situation, the first two dominant K–L modes would correspond to the first and third physical modes respectively.

It is to be noted that Set I, Case 1, represents a clamped–simply supported linear beam and Set I, Case 12, is a different linear system, namely, one that is merely clamped at one of its ends and free at the other. In both cases, only one K–L mode is dominant, but for cases in between the system is non-linear as is evidenced by the transfer of energy to higher K–L modes. The transition in the K–L modes from the physical modes of one linear system to the other is interesting. Only the general trends observed across the two sets of simulations are discussed here (Figure 4).

In Set I, the harmonic forcing is away from the point where vibroimpacts occur. The changes of the K–L mode shapes are very sensitive to the magnitude of the clearance. Figure 2(a–f) reveal that even for small clearance changes, the mode shapes look drastically different for the same value of the forcing frequency. Moreover, there is a propensity for many modes of the beam to be excited, as the location of the forcing is such that it does not fall on any of the nodes of the first several physical modes of the corresponding linear system. When the forcing frequency is low, the impacts are intermittent (smaller number of impacts), and the mode shapes are nearly invariant even when the clearance is changed. In this case, the non-linear effects are weak and no significant transfer of energy between the K–L modes takes place. As the forcing frequency increases, and the impacts are more frequent, the deformation of the mode shapes is greater (Frequency Index [5–15] of Figure 2(d)). These changes are more dramatically manifested in the second mode shapes as can be seen in Figure 3. This deformation of the K–L modes is caused by the strongly non-linear

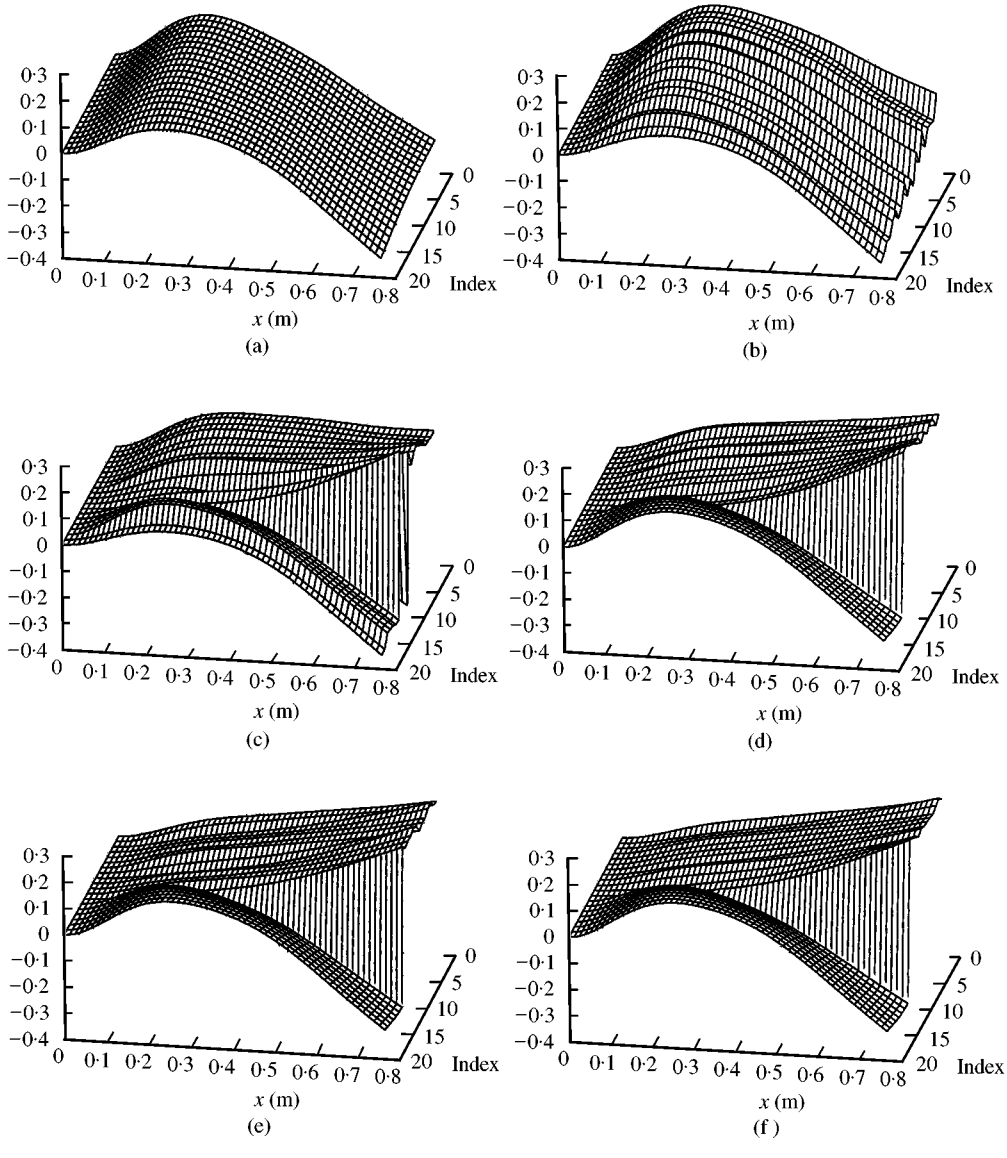

Figure 2. Set I (Mode I): (a) Case 1, (b) Case 3, (c) Case 5, (d) Case 7, (e) Case 9, (f) Case 11. Index refers to the frequency index tabulated in Table 4.

effects due to the vibroimpacts, which cause non-linear transfer of energy from low to high K–L modes. As the forcing location (f) is moved closer to the point of impacts, the mode shapes are less sensitive to the clearance. This is the reason why larger clearance steps are used in Set II of the simulations.

3.3. ENERGY TRANSFER BETWEEN K–L MODES

Here we discuss how the energy contents in each of the K–L modes are changed, as the parameters of the system change. The simultaneous study of the mode shapes and energy transfers between them, gives significant insight into the non-linear effects induced by the

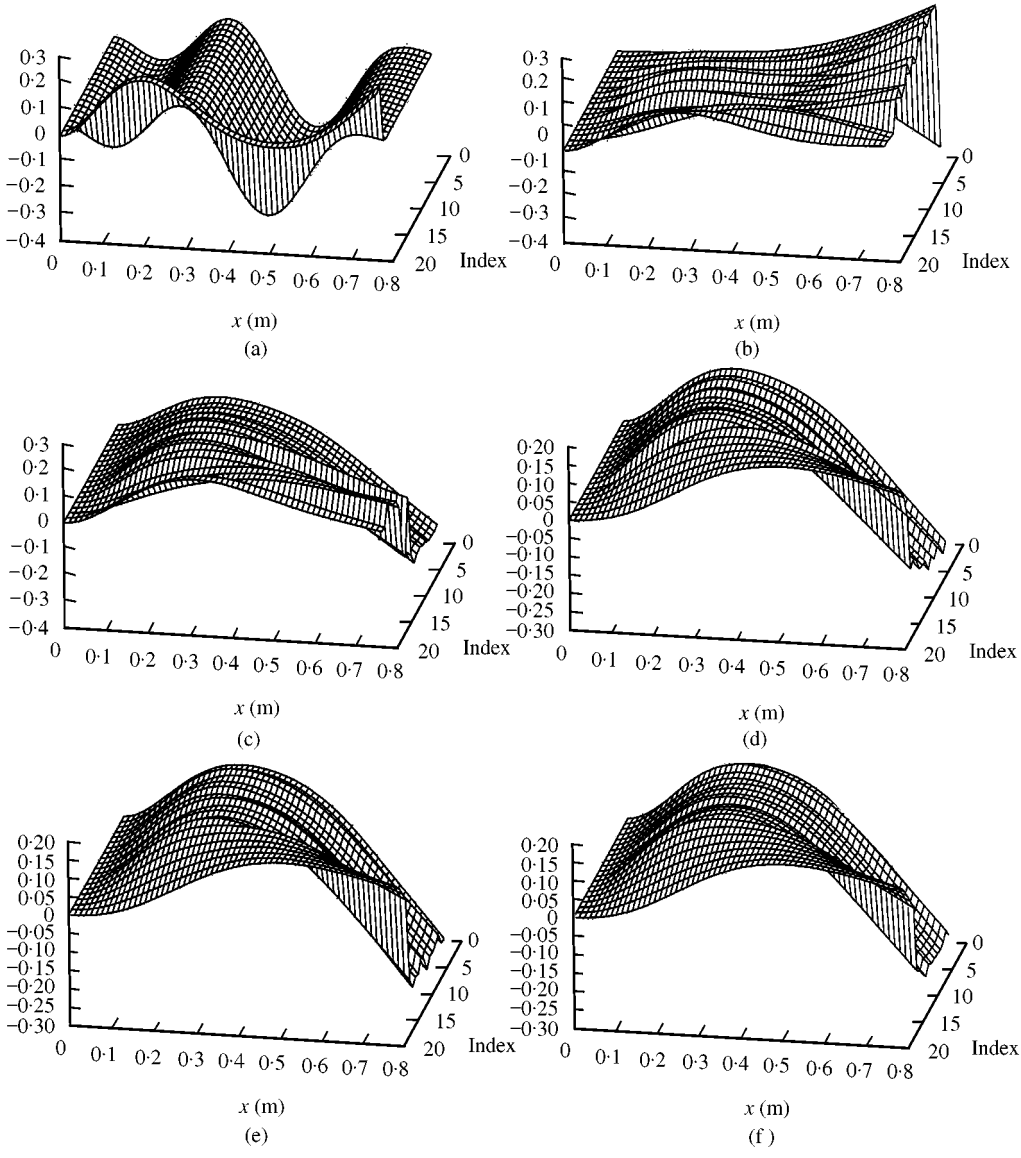

Figure 3. Set I (Mode II): (a) Case 1, (b) Case 3, (c) Case 5, (d) Case 7, (e) Case 9, (f) Case 11. Index refers to the frequency index tabulated in Table 4.

vibroimpacts in the beam. A typical energy diagram is shown in Figure 5. In this diagram, the energy percentage (equation (18)) in the first three K–L modes are plotted for varying forcing frequencies. For each set, many of these slices corresponding to each case are assembled in the surface plots shown in Figures 6 and 7. These plots can be used to get a measure of the dimensionality of the system. It can be seen that as the forcing frequency increases, due to the increase in impacts, the non-linear effects become more pronounced and energy transfer between low- and high-order K–L modes is increased. At higher forcing frequencies (away from the natural frequency), the amplitude of motion of the beam is low and hence there are no impacts; the response of the beam is then linear and nearly all vibrational energy is captured by a single K–L mode. This behavior occurs in a range of

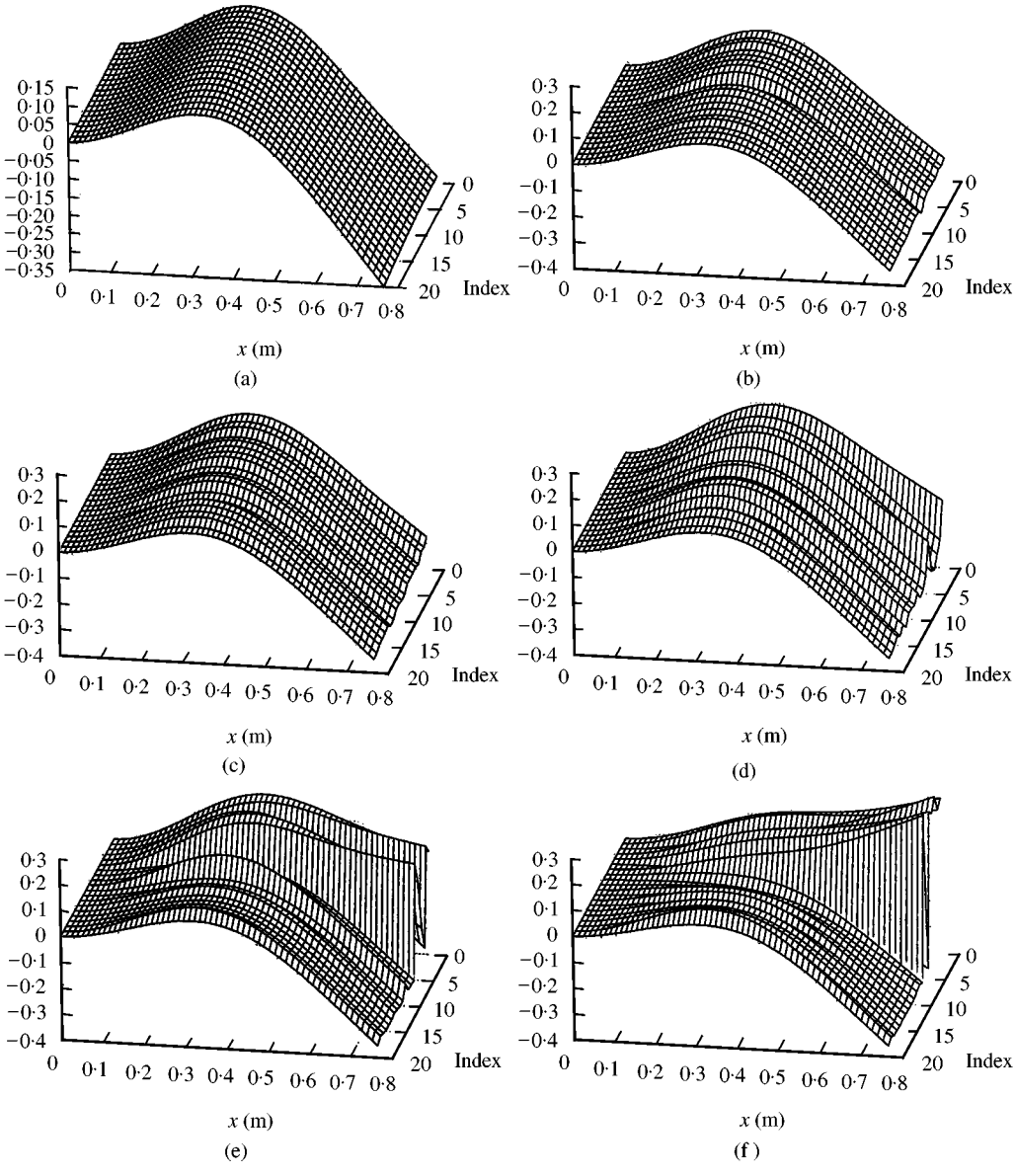

Figure 4. Set II (Mode I): (a) Case 1, (b) Case 3, (c) Case 5, (d) Case 7, (e) Case 9, (f) Case 11.

frequencies as can be seen from zone AB of Figure 5(a). When the forcing frequency is increased beyond that of point B, the system is moving towards the second natural frequency leading to an increase of the amplitudes and hence impacts start to occur. This is manifested as a drop in the energy of the first mode. The onset of this zone occurs at lower forcing frequencies when the clearance is increased, as in point A of Figure 5(b).

4. RECONSTRUCTION OF DYNAMICAL RESPONSE

A key advantage of obtaining the dominant K–L modes is that they can be used to construct lower order dynamical models for the system under consideration. If there is

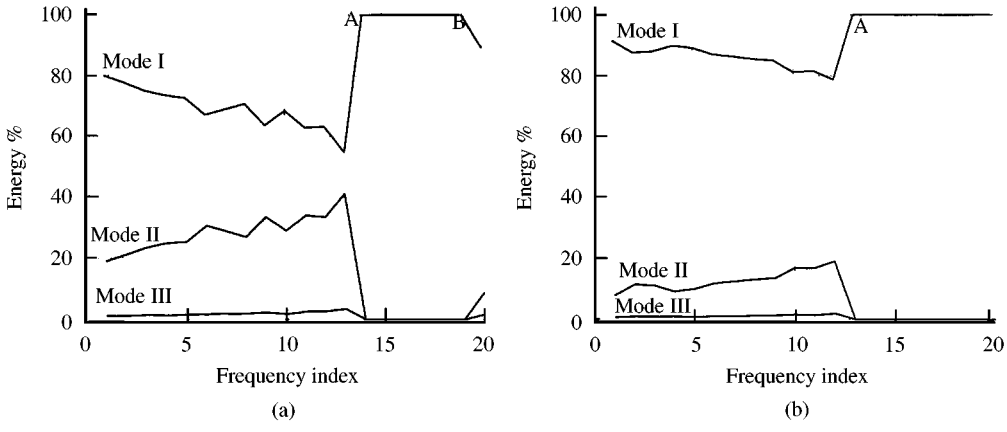

Figure 5. Typical K–L energy plot: (a) Set I, Case 6; (b) Set I, Case II.

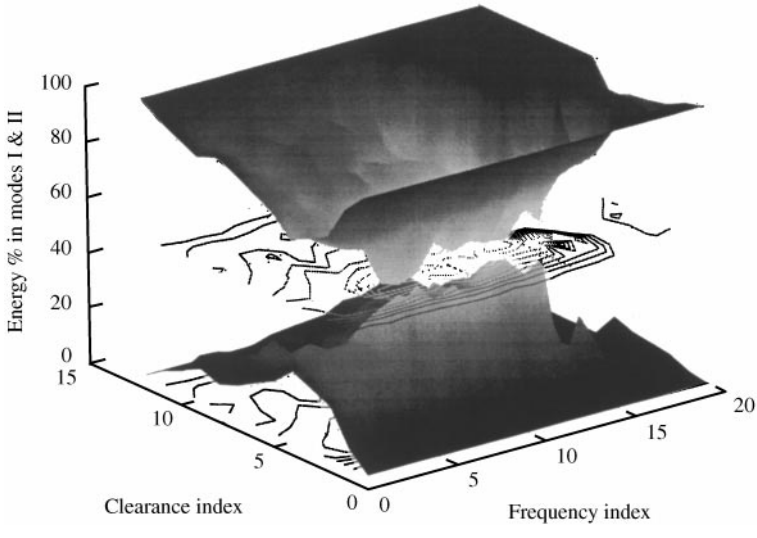

Figure 6. Surface K–L energy plot for Set I.

a large-scale structure, its response can be simulated using finite element models using traditional shape functions. Once a reasonable amount of data is obtained, the K–L modes can be extracted from them and lower dimensional models can be constructed which would result in tremendous saving of computational time. These lower order models can then be used for dynamical studies of structural modifications or for control system design. This procedure will be referred to as *reconstruction*. In this section, lower dimensional models are created for the non-linear beam considered so far, with impacting or higher order non-linearities, and both the original and reconstructed responses are shown for comparison purposes.

The governing PDE of the cantilever beam is given by

$$EI\frac{\partial^4 u}{\partial x^4} + m\frac{\partial^2 u}{\partial t^2} + d\frac{\partial u}{\partial t} = P(u,t)\delta(x-v) + F\cos(\Omega t)\delta(x-f), \tag{20}$$

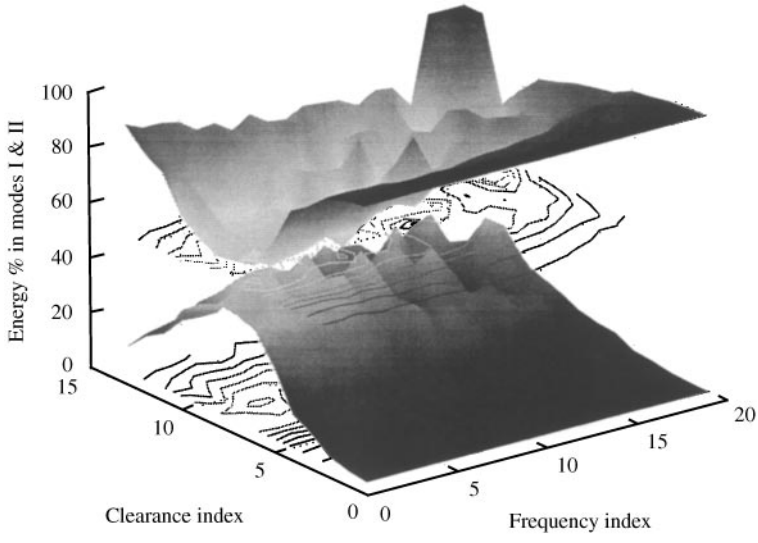

Figure 7. Surface K–L energy plot for Set II.

where $u = u(x, t)$ is the transverse displacement of the beam, $\delta(x)$ is the Dirac Delta distribution and the other parameters have the usual meaning. The force $P(u, t)$, due to the non-linear spring at $x = v$, is given by

$$P(u, t) = K_i(|u| - c)\frac{u}{|u|} \quad |u| > c \quad \text{for impacting spring,} \tag{21}$$

$$P(u, t) = K_\alpha \left(\frac{u}{c}\right)^\alpha \quad \text{for weakly non-linear spring,} \tag{22}$$

where c is the clearance at the point of impact and K_i is the impact stiffness for the impacting spring. The equation is defined on a domain $\Omega = [0, L]$. A solution of the form $u(x, t) = \sum_{i=1}^{p} \phi_i(x) a_i(t)$ is sought, where $\phi_i(x)$ are the set of admissible functions that satisfy the essential boundary conditions [21] of the problem. Here the K–L modes are used as this set of functions. The K–L modes are an ideal choice for this operation, because they satisfy natural and essential boundary conditions, as well as the orthogonality condition given by $\int_0^L \phi_i(x)\phi_j(x)\,\mathrm{d}x = c_j\delta_{ij}$, where δ is the Kronecker delta. Substituting this expansion in equation (20) one obtains

$$EI \sum_{i=1}^{p} \phi_i''''a_i(t) + m \sum_{i=1}^{p} \phi_i \ddot{a}_i(t) + d \sum_{i=1}^{p} \phi_i \dot{a}_i = P\delta(x - v) + F\cos(\Omega t)\delta(x - f). \tag{23}$$

Multiplying equation (23) by $\phi_j(x)$, integrating by parts over the domain (to reduce the order of the highest derivative) and employing the orthogonality conditions, the following set of discretized ordinary differential equations is obtained:

$$mc_j\ddot{a}_j + dc_j\dot{a}_j + EI \sum_{i=1}^{p} \xi_{ij}a_i = F\cos(\Omega t)\phi_j(f) + P\phi_j(v), \tag{24}$$

where

$$\xi_{ij} = \phi_j(L)\frac{\mathrm{d}^3\phi_i(L)}{\mathrm{d}x^3} - \frac{\mathrm{d}\phi_j(L)}{\mathrm{d}x}\frac{\mathrm{d}^2\phi_i(L)}{\mathrm{d}x^2} + \frac{\mathrm{d}\phi_j(0)}{\mathrm{d}x}\frac{\mathrm{d}^2\phi_i(0)}{\mathrm{d}x^2} + \int_0^L \frac{\mathrm{d}^2\phi_i(x)}{\mathrm{d}x^2}\frac{\mathrm{d}^2\phi_j(x)}{\mathrm{d}x^2}\,\mathrm{d}x. \qquad (25)$$

It is also noted that the boundary conditions are satisfied automatically by the K–L modes and need not be explicitly satisfied. Equation (24) represents a set of $2p$ ordinary non-linear differential equations. This can be numerically integrated using the FORTRAN SLATEC Runge–Kutta solver DDERKF as an initial value problem, or by employing high order schemes for stiff systems such as the Gear–Petzold (IMSL routine DIVPAG) or Gear–Adam–Moulton schemes. In the simulations performed here the Gear–Petzold scheme was used, with attention being payed to the detection of discontinuities and adjusting the time steps adaptively to accurately capture its effects. It should be noted that the K–L modes are available at discrete points in the domain. Hence, smooth B-spline interpolation functions of sixth order are created using the IMSL subroutine [22] DBSINT, to render a continuous mode shape in Ω. Once the interpolation coefficients are obtained, the routine DBSDER is used to compute the derivatives required in equation (24). The integrals are evaluated using the SLATEC routine DAVINT. It is advisable to employ double-precision computations throughout to reduce the numerical inaccuracies as much as possible. The number of K–L modes used (p) should be in accordance with equation (18). For the want of enhanced accuracy, the higher K–L modes should not be carelessly used as some of them are spurious and would lead to numerical instabilities. Consider the following example: if six physical cantilever modes were used to discretize and solve the system and if the resulting time domain data were used to obtain the K–L modes, one could obtain greater than six K–L modes if the method of Sanpshots is employed; the modes higher than the sixth mode would be numerical noise and should be considered as spurious. The criterion used to select non-spurious modes will be mentioned in the next section.

4.1. WEAKLY NON-LINEAR SYSTEM

The reconstructions are performed for two cases: weakly non-linear and impacting systems. In Figure 8 three K–L modes of a system corresponding to $f = 0{\cdot}1$ m, $c = 5$ mm, $\Omega = 52{\cdot}4$ rad/s, $\alpha = 3$ and $K_\alpha = 50$ N, are used to reconstruct the dynamical response of a system with different clearance and frequency ($c = 3$ mm, $\Omega = 30$ rad/s) and the comparison is shown in Figure 8(a). If p K–L modes of a system capture 99·9% of the

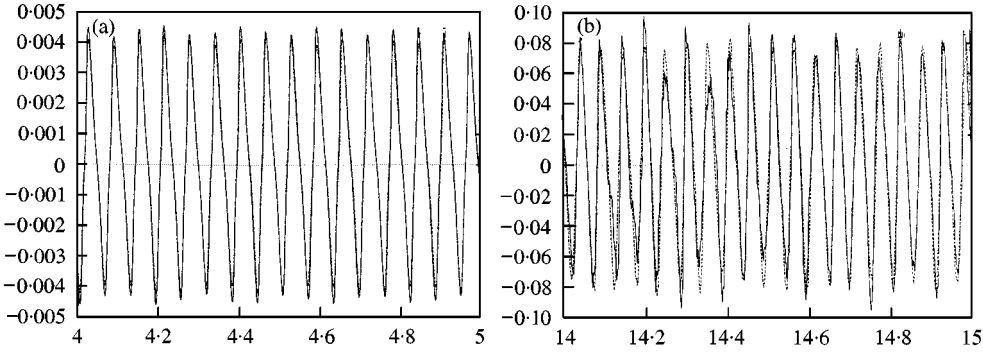

Figure 8. Comparisons of simulated (– – – –), and reconstructed (——) responses.

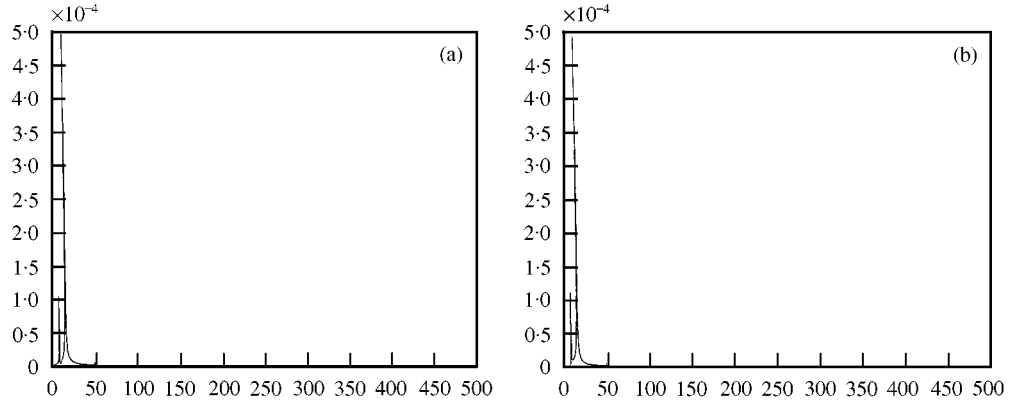

Figure 9. Comparisons of power spectra: (a) reconstructed and (b) simulated response.

energy, then the lower dimensional systems, with the same parameters, which are created using these modes will exhibit dynamics identical to the original system; however, there is no such guarantee if the lower dimensional systems are used to reconstruct the dynamics of a system with different parameters. The general observation is that the comparisons are good for small parameter changes. In cases where they do not compare well, one may use additional K–L modes for the reconstruction.

When vibroimpacts are involved, it is not always possible to obtain pointwise time domain convergence due to sensitive dependence on initial conditions. In such a situation the responses are compared in the frequency domain. For continuous systems undergoing vibroimpacts very small time steps have to be used for integration to get exact repeatability. This might not be feasible all the time and is not required. The comparisons in the frequency domain give an idea of the frequency content that each signal captures. The power spectra of the actual and reconstructed responses are shown in Figure 9 for a simulation in which $f = 0{\cdot}1$ m, $c = 5$ mm and $\Omega = 52{\cdot}4$ rad/s using only three K–L modes.

5. OVERHUNG ROTOR WITH VIBROIMPACTS

The schematic of the rotor with the definition of the various parameters is shown in Figure 10. The global dynamics of this system have been studied in depth in references [17, 23]. The parameters of the rotor are presented in Table 5; EI and m are the flexural rigidity and the linear mass density of the shaft, M_D the mass of the disk, I_D the diametrical moment of inertia of the disk, $d_{x,y}$ the damping constants of the shaft, L the length of the rotor, c the clearance at the point of impact $x = a$ and m_e is the unbalance mass at a radial location of e. The governing PDEs of the rotor including the gyroscopic moments and gravity effects of the disk are given as

$$EI\frac{\partial^4 u_1}{\partial x^4} + m\frac{\partial^2 u_1}{\partial t^2} + M_D\,\delta(x-L)\frac{\partial^2 u_1}{\partial t^2} + 2\Omega I_D\frac{\partial^2 u_2}{\partial x\partial t}\,\delta'(x-L) + d_x\frac{\partial u_1}{\partial t}$$

$$= P_1(t)\delta(x-a) + Q_1(t)\delta(x-L),$$

$$EI\frac{\partial^4 u_2}{\partial x^4} + m\frac{\partial^2 u_2}{\partial t^2} + M_D\,\delta(x-L)\frac{\partial^2 u_2}{\partial t^2} + 2\Omega I_D\frac{\partial^2 u_1}{\partial x\partial t}\,\delta'(x-L) + d_y\frac{\partial u_1}{\partial t}$$

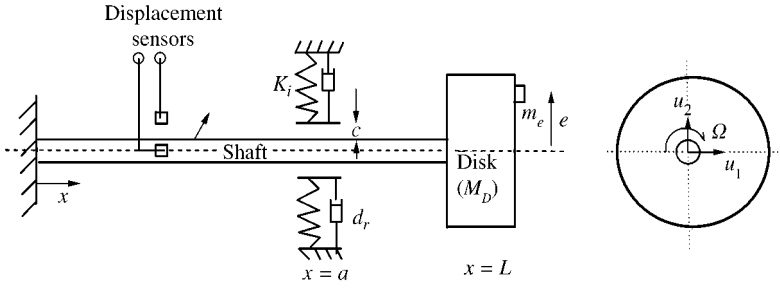

Figure 10. Schematic of the overhung rotor.

TABLE 5

Parameter values of the vibroimpact overhung rotor

Parameter	Value	Parameter	Value
a	0·5064 m	c	1·5 mm
d_x	1·0 N s/m^2	d_y	1·0 N s/m^2
EI	128·97518 N m^2	e	0·05 m
I_D	$5{\cdot}4032 \times 10^{-4}$ kg m^2	K_i	10^8 N/m
L	0·635 m	M_D	0·8375 kg
m	1·14628 kg/m	m_e	0·03 kg

$$= P_2(t)\delta(x-a) + Q_2(t)\delta(x-L),$$

$$u_{1,2}(0,t) = \frac{\partial u_{1,2}}{\partial x}(0,t) = 0, \qquad \frac{\partial^2 u_{1,2}}{\partial x^2}(L,t) = \frac{\partial^3 u_{1,2}}{\partial x^3}(L,t) = 0, \tag{26}$$

where $u_1(x,t)$ and $u_2(x,t)$ are the displacements in the vertical and horizontal directions respectively; $P_{1,2}$ the forces due to clearance impacts and $Q_{1,2}$ the external forces acting on the disk, given by

$$Q_1(t) = m_e\Omega^2 e\cos(\Omega t), \qquad Q_2(t) = m_e\Omega^2 e\sin(\Omega t) - M_D g$$

$$P_1(t) = -\xi\left(K_i\frac{(r-c)u_1}{r}\right), \qquad P_2(t) = -\xi\left(K_i\frac{(r-c)u_2}{r}\right), \tag{27}$$

where $\xi = 1$ if $r \geqslant c$, $\xi = 0$ if $r < c$, and $r = \sqrt{u_1^2 + u_2^2}$.

The dynamics of the system are numerically obtained by using the mode shapes of a cantilever beam with a mass at the end to discretize the PDEs.

5.1. K–L MODE SHAPES AND ENERGY TRANSFER DIAGRAMS

The K–L modes and energies are obtained for 12 cases of varying clearance shown in Table 6. For each of these cases the speed of rotation is varied from 400 to 4000 r.p.m. as shown in Table 7. The different clearance and speed values are referred to by the case numbers (Table 6) and speed indices (Table 7) respectively.

TABLE 6

Parameters for rotor simulation

Case no.	1	2	3	4	5	6	7
c (mm)	0·001	0·2	0·4	0·6	0·8	0·9	1·0
r_a (m)	0·6064	0·6064	0·6064	0·6064	0·6064	0·6064	0·6064
Case no.	8	9	10	11	12	13	14
c (mm)	1·2	1·4	1·6	1·8	2·4	1·0	1·0
r_a (m)	0·6064	0·6064	0·6064	0·6064	0·6064	0·4064	0·5064

TABLE 7

The different speeds at which simulations are performed are represented by indices

Frequency index	1	2	3	4	5	6	7	8	9	10
Ω (rpm)	400	500	600	700	800	900	1000	1100	1200	1300
Fraequency index	11	12	13	14	15	16	17	18	19	20
Ω (rpm)	1400	1500	1600	1700	1800	1900	2000	2100	2200	2300
Frequency index	21	22	23	24	25					
Ω (rpm)	2400	2600	2900	3200	4000					

There are two displacements at each point on the shaft (vertical and horizontal ones): these data are processed independently to obtain the *horizontal* and *vertical* K–L modes of the system. The first K–L mode shapes for a few cases of Table 6 are presented in Figure 11. At low speeds, the shaft just rides on the lower surface of the bearing (with clearance) because of the weight of the disk. There are no violent impacts, as the inertia is not sufficient for the shaft to impact violently all over the bearing. Hence, even though there are "weak" impacts, the shaft amplitudes are not high and the K–L mode shapes resemble the first physical mode of a cantilever beam. Clearly, at low speeds the rotor dynamics is approximately linear, and a single K–L mode dominates the response; transfer of energy to higher K–L modes is minimal.

As the speed is increased, the harmonic forcing acting on the system also increases due to the mass unbalance, and the vibroimpacts occur vigorously. This leads to a bending of the K–L mode shapes, and the first K–L mode now resembles the second physical mode of a cantilever beam. At the same time, the second mode (not shown in figures) changes and appears to be similar to the first physical mode. It can also be seen that at certain speeds the second K–L mode resembles the third physical mode. At these speeds, the first physical mode does not dominate the response and may (or may not) appear as being a higher, less dominant K–L mode. In the case of larger clearance, violent impacts do not occur until very high speeds are reached, a phenomenon that is manifested as less-sensitive K–L mode shapes.

The energies of the K–L modes, corresponding to all cases indicated in Table 6, are shown in Figures 12 and 13. The time traces of a few of the simulations (marked as numbers on these plots) are reproduced in Figure 14 (with the corresponding numbers on the top right corner of the latter plots). Consider, for example the energy plot of Case 6. It can be seen that there is no demarcation of regions of high (or low) energy transfer, as with the impacting beam. The reason is that, the rotor system, has many factors coming into play,

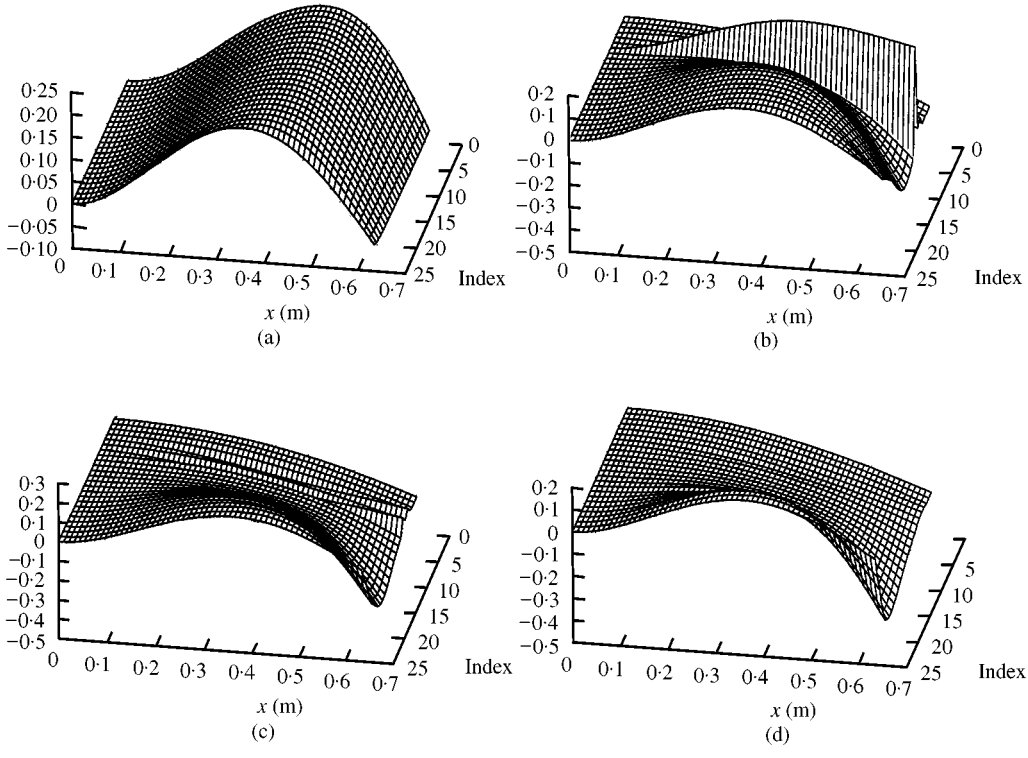

Figure 11. First horizontal K–L mode of the overhung rotor: (a) Case 1, (b) Case 3, (c) Case 7, (d) Case 10.

like, the gyroscopic interactions, the participation of many modes and the shaft–disk interactions. It was shown in reference [23], that unexpected solution changes take place in this system in the form of chaotic explosions. The questions arising at this point are; how does the response affect the energy transfer?, Or the inverse problem, namely, what can be said about the responses from a given energy transfer plot? These are important questions that need to be answered if this method is to be used for diagnostics.

A few trends observed from the simulations are described now, in reference to Figures 12 and 13. For almost zero clearance, most of the energy is captured only by one K–L mode at all speeds of rotation. This is because the system is essentially linear. As the clearance increases, the amount of energy transfer also increases drastically. But there seems to be a critical value of clearance ($c = 1$ mm) when the energy transfer is at its maximum. This seems to be a critical value of clearance for which non-linear effects in the system due to vibroimpacts are more pronounced. Note that by increasing or decreasing the clearance from this critical value, one approaches two limiting *linear* systems. Moreover, the participation of the higher modes is also enhanced close to this clearance value. After this critical value, the energy transfer decreases as the system is now transitioning to a linear system that corresponds to an overhung rotor without any supporting bearing. This is an important result, as it shows, how much the clearance can be increased without having catastrophic effects. In practical situations involving journal bearings, the clearance cannot be too small, because enough oil flow cannot be maintained to counteract friction. On the other hand, a larger clearance gives rise to large-amplitude motions and high stresses in the elements. When the clearance is very large, there are no impacts and hence the system behaves like a linear one. An ideal clearance can be selected based on the critical value

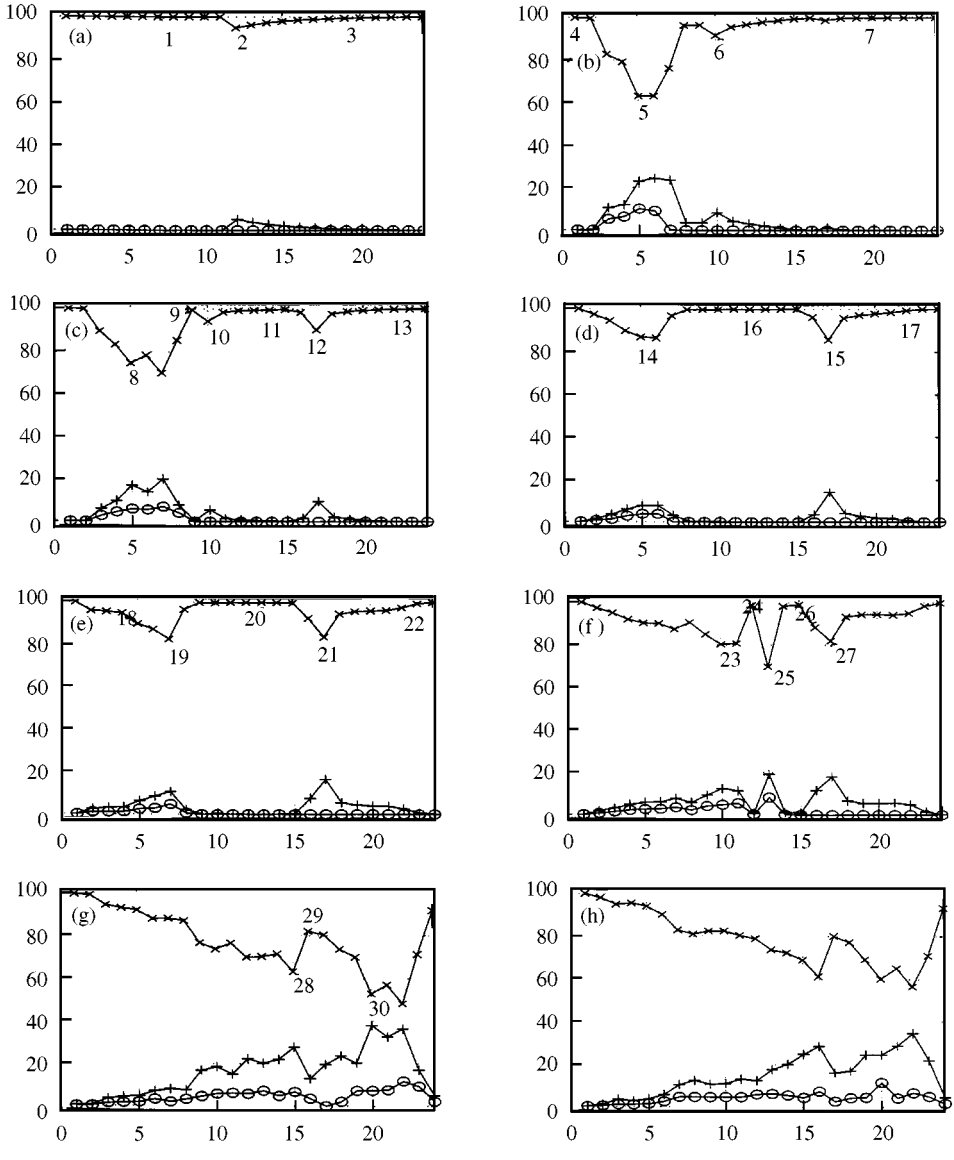

Figure 12. Percentages of K–L energies in the three leading K–L modes: (a) Case 1, (b) Case 2, (c) Case 3, (d) Case 4, (e) Case 5, (f) Case 6, (g) Case 7, (h) Case 8; —×—, Mode I; —+—, Mode II; —○—, Mode III.

obtained by a K–L analysis. This trend where the system moves from one linear system to another, with maximal nonlinearity effects for a system in between, is observed also for the vibroimpacting beam example (Figure 6).

It can be seen from the orbits in Figure 14 that whenever the motion is periodic (for example point 7) there is only one dominant K–L mode. However, if the motion of the rotor is chaotic there is more K–L mode participation and larger transfers of energy from the first to the second K–L mode occur (points 5, 8, 33). For all other types of non-linear responses, such as subharmonic (6, 34) or quasiperiodic (36) motions, there is moderate energy transfer between the K–L modes. It can be seen from these energy transfer diagrams, that there are no well-defined regions where the energy transfer is high or low. The transfer of energy

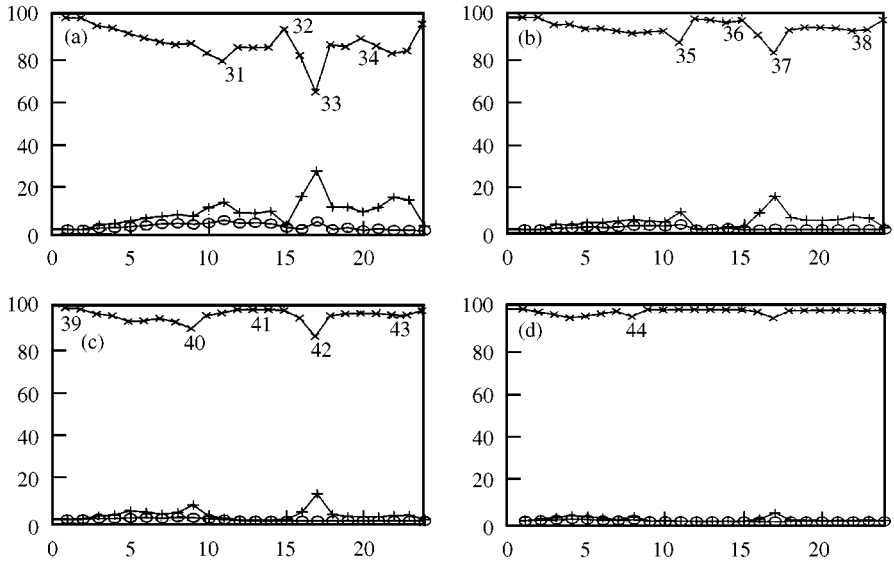

Figure 13. Percentages of K–L energies in the three leading K–L modes: (a) Case 9, (b) Case 10, (c) Case 11, (d) Case 12; —×—, Mode I; —+—, Mode II; —○—, Mode III.

varies erratically as can be seen from points 23 through 27. This fact ties well with the observation of chaotic explosions, and sudden appearances of periodic solutions [24]. It can be seen that while in the periodic regimes only one K–L mode (points 1, 7, 11, 13) captures all the energy, more than three K–L modes are required for chaotic regions (points 5, 30, 29). Moreover, this behavior was consistent in all simulations performed.

5.2. RECONSTRUCTION OF RESPONSE

We now show how the computed K–L modes can be used to create low-dimensional models of a system that can capture the dynamics more accurately than conventional Galerkin procedures based on linearized modes. Here the PDEs governing the motion of the rotor are discretized using the K–L modes as trial functions instead of using the linearized mode shapes as done in references [24, 23]. The procedure for reconstruction of the rotor responses is similar to that used for the beam example of Section 4. The only difference is that there is a shear force discontinuity at $x = L$. This is not captured by the K–L modes and has to be manually enforced. This is represented as

$$\phi_i'''(x = L) = 0, \tag{28}$$

where ϕ_i are the vertical or horizontal K–L modes.

Here six different cases of reconstructions are performed as listed in Table 8. The following discussions are in reference to this table and Figure 15. In Cases 1 and 2, the motion is periodic and only one K–L mode can capture the exact response (Figure 15). Cases 3–6 correspond to the bilinear stiffness model for the intermediate spring [see $P_{1,2}(t)$ in equation (27)] with varying degrees of stiffness coefficients. The responses of Case 3 are neither periodic nor chaotic and there are mild impacts occurring. In this case, even though three K–L modes capture 99·9% of the energy, only the first two are used in the

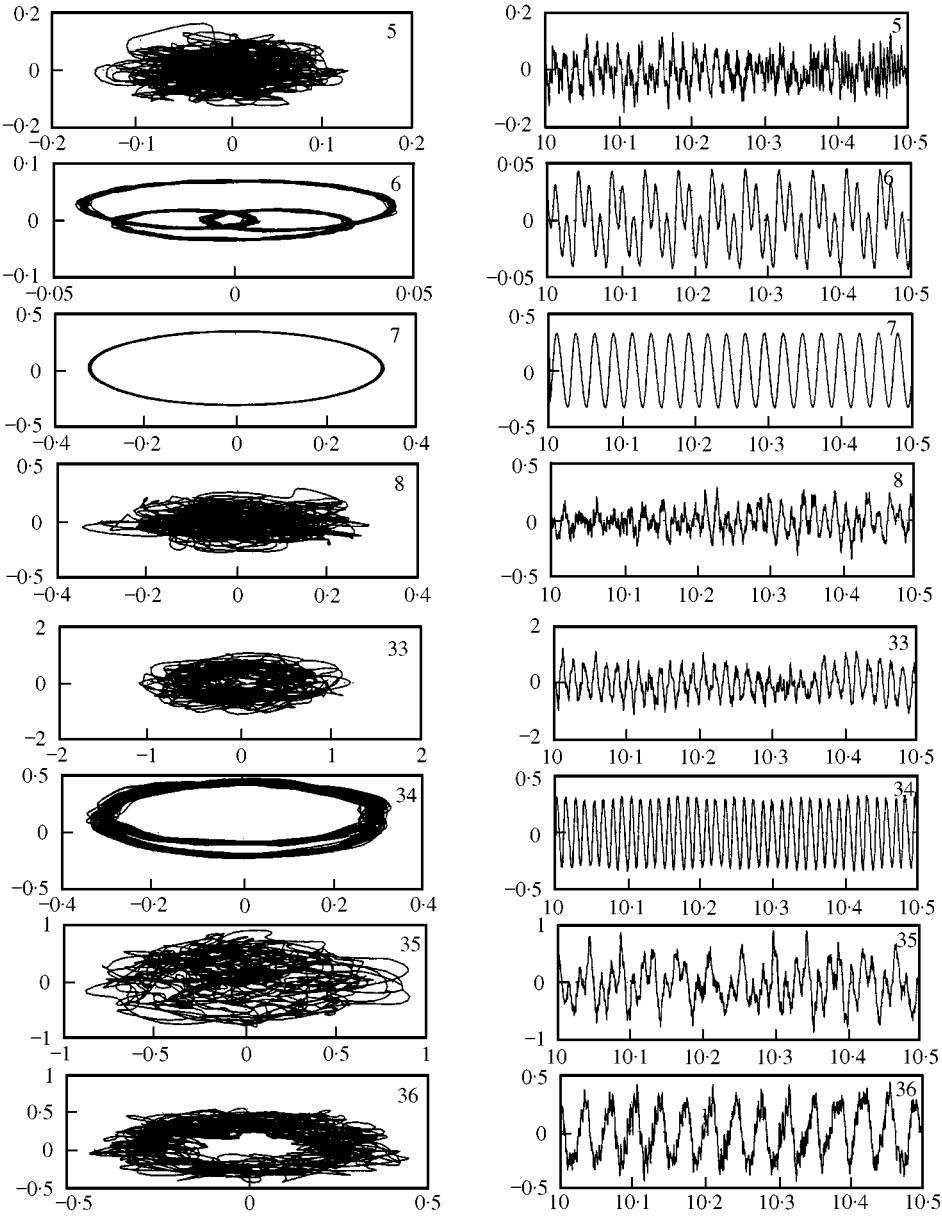

Figure 14. Orbits and horizontal displacements (in mm) for the points at the rotor marked in Figures 12 and 13 at $x = 0{\cdot}302$ m.

reconstruction. The trends and amplitudes of the exact response are captured accurately by the reconstruction. In Case 4, the motions are chaotic and four K–L modes are needed to capture the response. Cases 5 and 6 are essentially periodic and four K–L modes are used for the reconstruction. This is an overkill, as only one K–L mode captures almost all energy. But four modes are used to illustrate that the higher modes are not spurious and can still be used as trial functions. This is important because if the K–L modes of one system have to be used to reconstruct the dynamics of a slightly different system then the higher modes can be included to enhance the convergence.

TABLE 8

The parameters used in the reconstruction study

Case	Speed (r.p.m.)	Non-linear spring	a (m)	c (mm)	Number of K–L modes used
1	900	$10^6(u/c)^3$	0·4064	0·5	1
2	1200	$10^6(u/c)^3$	0·4064	0·5	1
3	1000	↑	0·6064	0·5	2
4	800	|	0·6064	0·2	4
5	1100	$10^8(u-c)(u>c)$	0·6064	0·5	4
6	2300	↓	0·6064	0·2	4

It is finally noted that even though six physical mode shapes of the corresponding linear system are needed to obtain correct responses, a maximum of four K–L modes only is needed for the same purpose. This might not appear to be a major saving of computational time. But consider a practical situation where a FEM model is used to model complicated rotor systems as considered in the case of a crankshaft in automotive engineering. In this case, the rigid disks representing the cams and nose are also discretized using several elements: even though the disks contribute to the dynamics as a whole, the individual discretized element's contribution is negligible and hence the degrees of freedom of the models are unnecessarily increased greatly. If the K–L method is applied to such a system it immediately provides a dimensional estimate which would significantly reduce the size of the problem and yet guarantee accurate results.

6. EXPERIMENTAL K–L PROCEDURE

In the previous section, the K–L modes of a rotor dynamic system with vibroimpacts were obtained from numerical data. There it was argued that the K–L modes and their energies can be used to predict certain types of non-linear behavior. It is the aim of this section to try and obtain qualitative comparisons between numerical simulations and experimental results for the same system. The important issue in obtaining good experimental modes, is the need for precise simultaneous measurement at different stations along the system. There are two notable works in the area of non-linear dynamics, where experiments are performed on beam systems. In reference [25], the dynamics of a coupled beam–pendulum oscillator were studied. Several accelerometers were mounted on the beam to obtain simultaneous measurement of accelerations, which were then processed to obtain the mode shapes. Using this method the first two K–L mode shapes are obtained very accurately. In this case, the use of acceleration fields to extract the mode shapes was acceptable, as there are smooth variations of the forces and moments along the beam as the system had smooth non-linearities. However, if there are vibroimpacts occurring in the system, accelerometers cannot be used and the situation calls for non-contact displacement measurements. If the amplitudes are small, contact means such as strain gauges and linear variable displacement transducers (LVDT) can be used. High speed cameras cannot be employed in this case as the physical dimensions of the set-up are large and such cameras can only capture simultaneous snapshots of limited areas of the structure.

The work carried out by Cusumano *et al.* [15] more closely represents the experiments carried out here. A clamped beam was impacted harmonically at its tip by means of a shaker

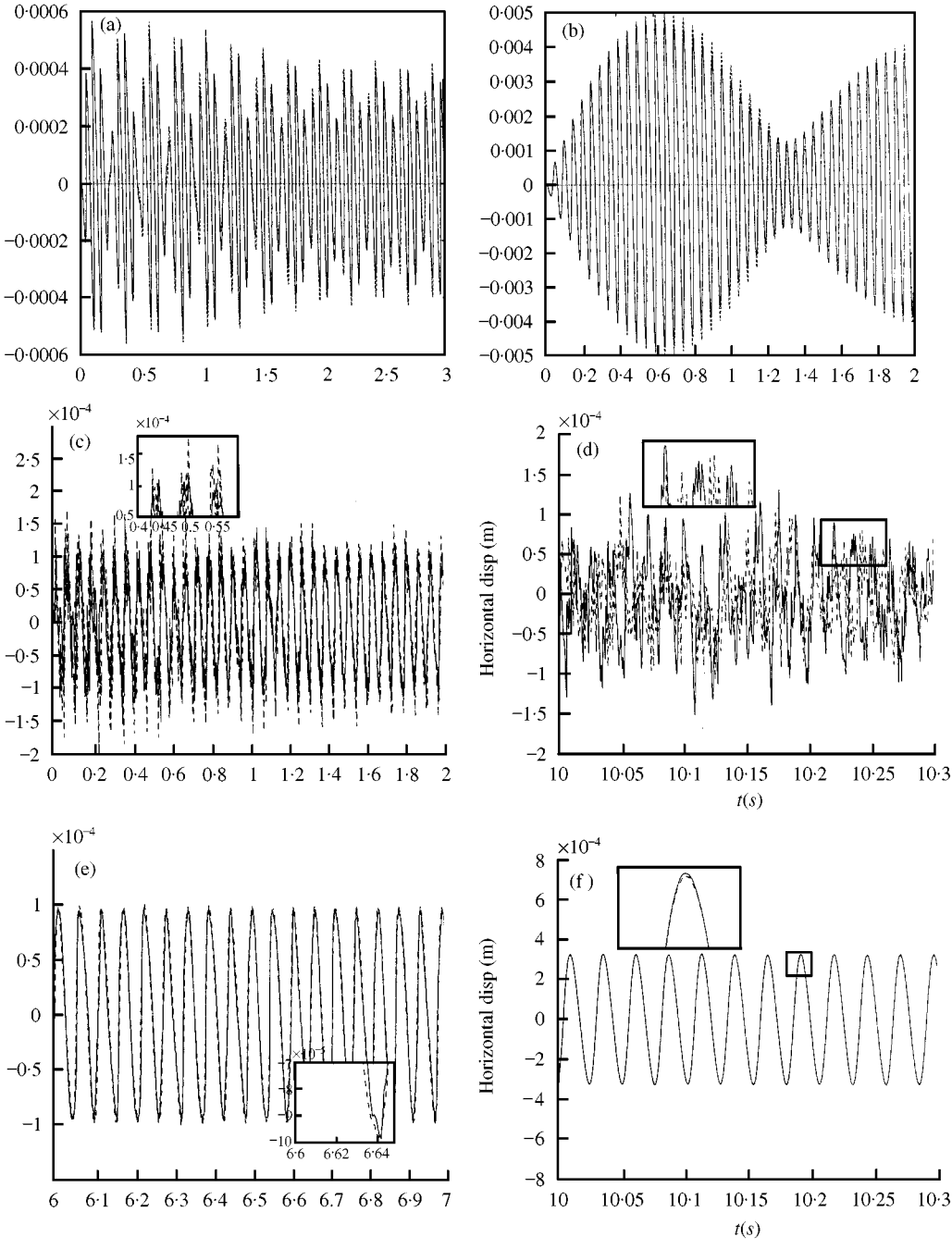

Figure 15. Sample reconstructions for Cases 1–6 of Table 8, reconstructed (– – – –), and exact (——) responses: (a) Case 1, (b) Case 2, (c) Case 3, (d) Case 4, (e) Case 5, (f) Case 6.

and dimensionality studies were performed using different methods such as K–L decomposition, Lyapunov exponents and fractal dimensions. In that experiment, two fiber-optic displacement probes were used to measure displacements at five points only, by restarting the experiment after the data at two points were acquired. It was mentioned, that

the manual movement of these sensors to the new locations precluded measurements at a higher number of points.

The rotor set-up examined herein has two major hurdles that are not present in the previous two works: (a) it is a rotating system with relatively large amplitudes, and (2) there is vibroimpact motion. Hence, accelerometers or eddy sensors cannot be used in this case. The only other means is to use a series of laser displacement sensors, but their cost is prohibitive. These problems have been circumvented by means of careful experimentation as will be explained in the next section.

6.1. EXPERIMENTAL FIXTURE AND PROCEDURE

The schematic of the experimental fixture is depicted in Figure 16 and a picture of the actual set-up is shown in Figure 17. The material and physical parameters of the rotor

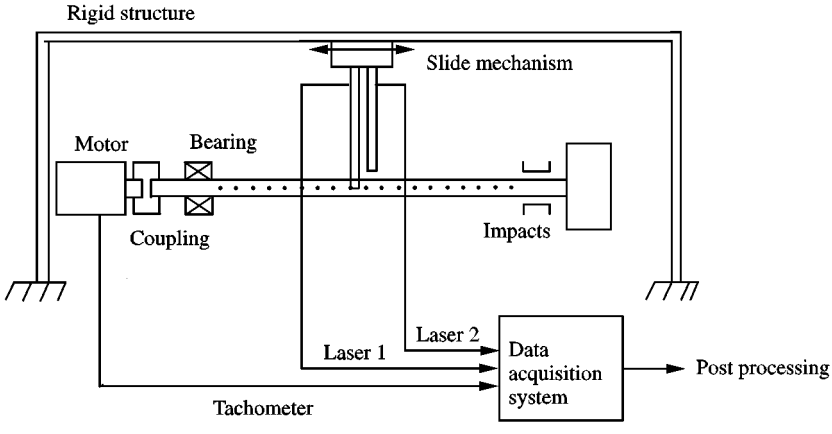

Figure 16. Schematic of the experimental set-up of the rotor.

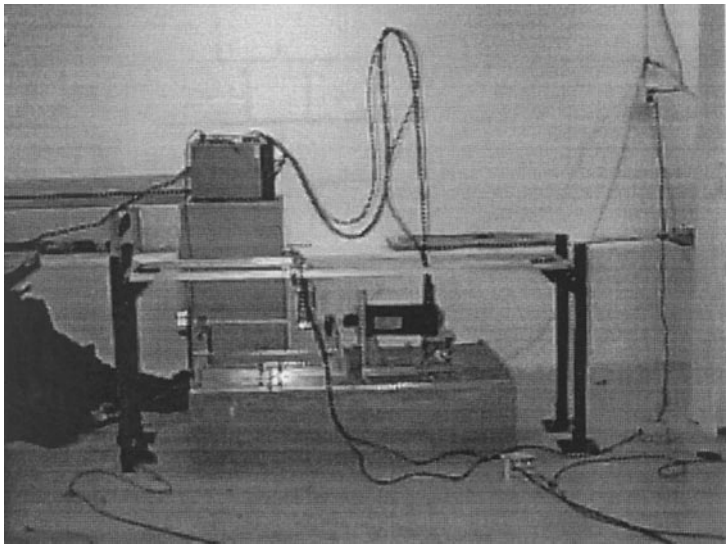

Figure 17. Picture of the experimental set-up.

considered here are identical to that used in the numerical simulations of Section 5 except for the length of the shaft and the distance between the two bearings. The new length is 55·9 cm (22″) and the new distance between the supports is 49·5 cm (19·5″). As can be seen, the new overhang length is only 1·5″. The unbalance mass used weighed 45 g and was located at a radial distance of 1″ from the shaft centerline. The measurements were made at 19 evenly spaced measurement points between the rotor bearings. The bandwidth of data acquisition used was 500 Hz with a resolution of 1024 lines per second. The displacement measurements at different points on the shaft cannot be made simultaneously: hence, the rotor is run at a certain speed, the measurements recorded, the laser moved to a different location and the experiment restarted by positioning the rotor at the same place as before. The initial conditions should be the same for each run, as different initial conditions lead to different responses, which would render the K–L procedure inapplicable. The data acquisition is triggered by means of a tochometer signal from the motor control unit. The first 100 cycles of the forcing frequency are rejected before the data are acquired, to give enough time for the transients to die out and steady state measurements to be performed.

6.2. EXPERIMENTAL K–L MODES

The experiments are performed for four different clearances and three speeds of rotation for each clearance. The corresponding K–L modes are computed using the method of snapshots, using 1024 snapshots. The modes are computed for both the horizontal and vertical time traces, and the energies corresponding to these modes are also obtained. Only results of the vertical K–L mode are presented here. The different experiments are identified by case indices, and the experimental parameters corresponding to each index are presented in Table 9.

The first and the second K–L modes for the various cases using the vertical time-series data are presented in Figures 18 and 19. Only the first and second mode shapes are presented, as the higher modes could not be obtained with sufficient accuracy. To better visualize the deformation of the experimental K–L for change in speed and clearance, a smooth fifth order polynomial is fit to the first K–L mode. These are compared in Figure 20 where the clearance is fixed and the modes are compared as the speed of rotation is varied. The energies contained in the first two modes, for the different cases shown in Figure 21, enable one to study energy transfers between the K–L modes and to verify the theoretical predictions of section 5.1.

Since the main reason for obtaining these K–L modes is to predict certain kinds of non-linear motion, it is necessary to have an idea of the dynamical behavior of the rotor response. Hence, the power spectra of the vertical displacement at $x = 15''$ for the various cases are presented in Figures 22 and 23. In the discussion that follows, all these figures will be referred to.

TABLE 9

The parameters for which experiments were performed

Case no.	1	2	3	4	5	6
Speed (r.p.m.)	900	1200	1400	900	1200	1400
Clearance (mm)	0·5	0·5	0·5	1	1	1
Case no.	7	8	9	10	11	12
Speed (r.p.m.)	900	1200	1400	900	1200	1400
Clearance (mm)	1·55	1·5	1·5	2	2	2

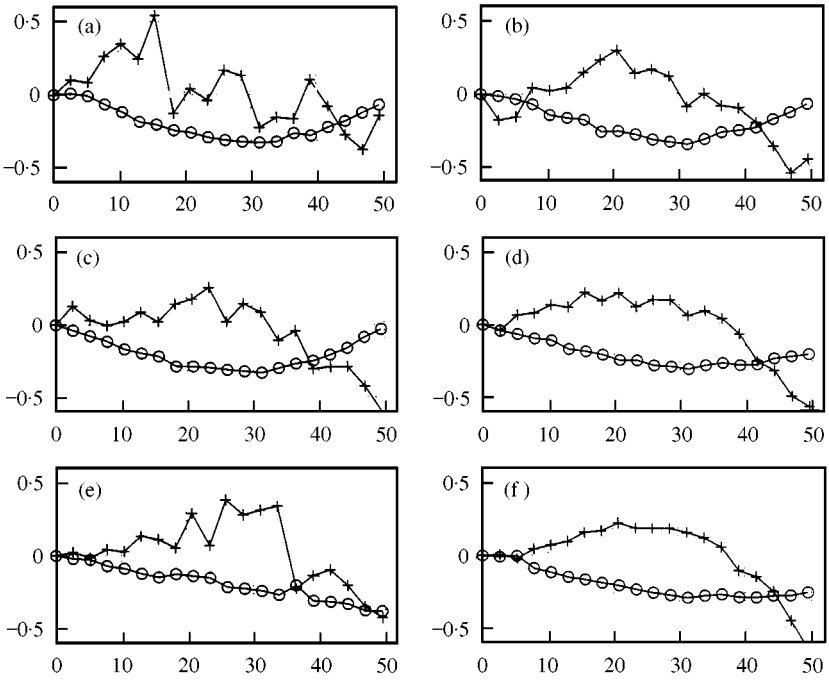

Figure 18. Vertical K–L modes for Cases 1–6: (a) Case 1, (b) Case 2, (c) Case 3, (d) Case 4, (e) Case 5, (f) Case 6; —○—, Mode I; —+—, Mode II.

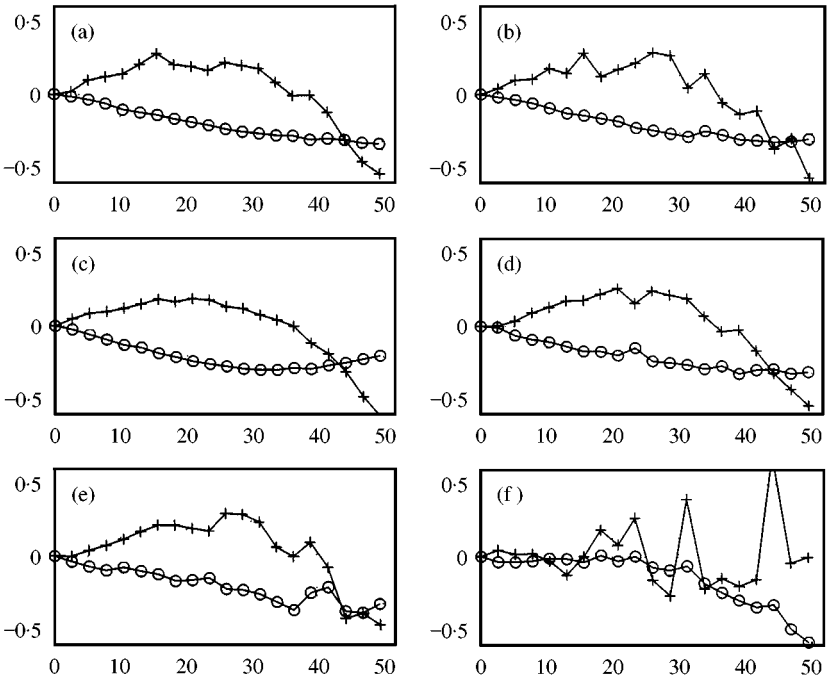

Figure 19. Vertical K–L modes for Cases 7–12: (a) Case 7, (b) Case 8, (c) Case 9, (d) Case 10, (e) Case 11, (f) Case 12; —○—, Mode I; —+—, Mode II.

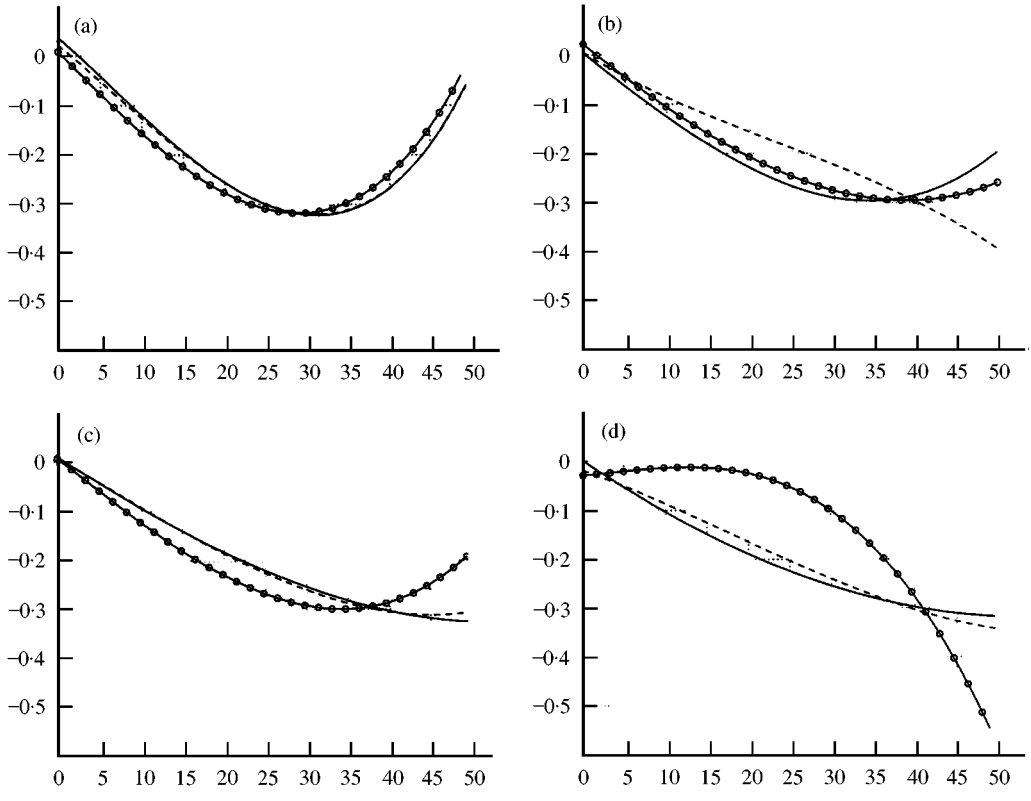

Figure 20. Variations in the experimental vertical K–L mode shapes as the speed of rotor rotation varies for clearances of (a) 0·5 mm, (b) 1·0 mm, (c) 1·5 mm, (d) 2·0 mm; ——, 900 r.p.m.; – – – –, 1200 r.p.m.; ○, 1400 r.p.m.

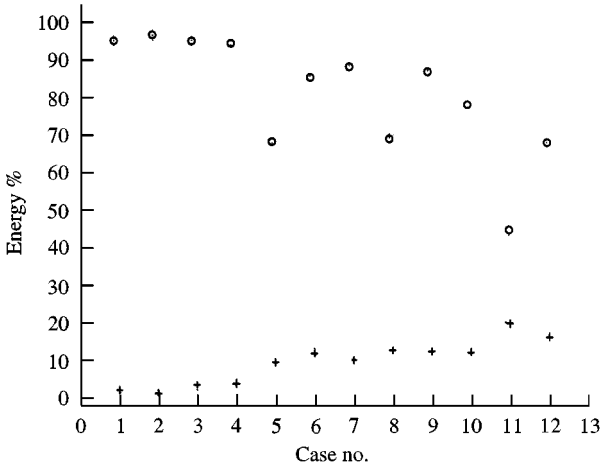

Figure 21. K–L Energy fractions for the cases listed in Table 9 for the vertical K–L modes: ○, Mode I; +, Mode II.

For a clearance of 0·5 mm, the motion remained almost periodic for the speeds under consideration. The reason is that at this value of clearance the closest linear system is a clamped–simply supported rotor. Hence, the critical speeds are much higher than those of

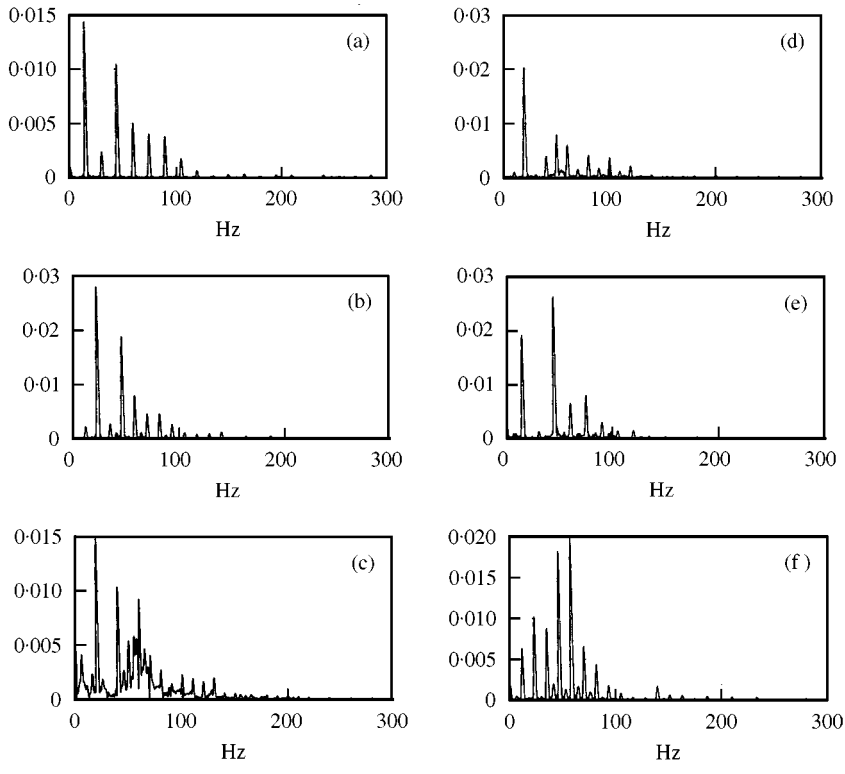

Figure 22. Power spectra of the experimental time traces for vertical displacements at $x = 10''$ for clearance and rotor speed: (a) 0·5 mm, 900 r.p.m.; (b) 0·5 mm, 1400 r.p.m.; (c) 1·0 mm, 1200 r.p.m.; (d) 0·5 mm, 1200 r.p.m.; (e) 1·0 mm, 900 r.p.m.; (f) 1·0 mm, 1400 r.p.m.; —○—, Mode I; —+—, Mode II.

an overhung rotor and the speeds used in the experiments are not enough to sufficiently excite the rotor for violent impacts to occur. Hence, the dominating K–L mode (Mode I) always resembles the first physical mode of a clamped–simply supported beam There are very mild impacts at 1400 r.p.m. In addition, there is little change in these mode shapes even as the speed is increased (Figure 20). This fact is confirmed from the corresponding energy transfers and power spectra (Figures 21 and 22). At a speed of 900 r.p.m. there are dominant peaks only at integral multiples of the forcing frequency (speed of rotation) and this suggests periodic motion (Figure 22). This could be the reason, that the second mode cannot be obtained accurately, since there is no sufficient energy transfer to sufficiently excite the higher K–L modes of the rotor. At higher speeds, however, there are signs of vibroimpacts.

As the clearance is increased to 1 mm impacts occur more readily (Figure 22). At 900 and 1400 r.p.m. the impacts are of smaller magnitude compared to those at a speed of 1200 r.p.m. At 1200 r.p.m. the vibroimpacts are severe and this results in a bending of the mode shape (Figure 20). This is also manifested as large energy transfers between the first and second K–L modes (Figure 21).

For a clearance of 1·5 mm, the response at 900 r.p.m. constitutes large but periodic impacts. In particular, the response is subharmonic of period-2, as can be seen from the appearance of sharp peaks in the corresponding power spectrum, at one-half the integral multiples of the forcing frequency (Figure 22). This type of response is due to the non-linear nature of the vibroimpacting rotor. The response at 1200 r.p.m. is chaotic and at 1400 r.p.m. settles to a periodic orbit. It can be seen from the comparisons of the K–L mode shapes that

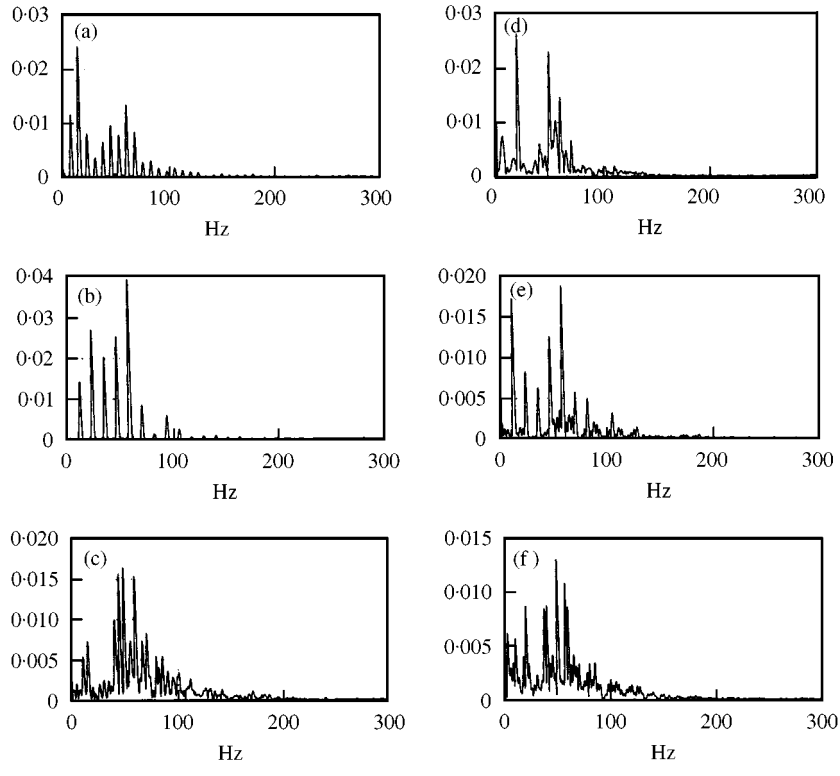

Figure 23. Power spectra of the experimental time traces for vertical displacements at $x = 10''$ for clearance and rotor speed: (a) 1·5 mm, 900 r.p.m.; (b) 1·5 mm, 1400 r.p.m.; (c) 2·0 mm, 1200 r.p.m.; (d) 1·5 mm, 1200 r.p.m.; (e) 2·0 mm, 900 r.p.m.; (f) 2·0 mm, 1400 r.p.m.; —○—, Mode I, —+—, Mode II.

their deformation is small for the case of periodic responses (Figure 20). These observations are also confirmed by the corresponding energy plot where there is a huge transfer of energy for the chaotic motion case (1200 r.p.m.) (Figure 21).

Lastly, the case of 2 mm clearance is considered. As the speed is increased, the severity of vibroimpacts also increases. At 1400 r.p.m., the impacts are very violent and have large amplitudes and this could be the reason why even the first mode shape could not be obtained accurately (Figure 20).

7. CONCLUSIONS

In this paper, the K–L method has been used to study the qualitative dynamics of vibroimpact systems and to create lower dimensional models. The method has been applied to a vibroimpacting beam and rotor. The viability of the use of the obtained K–L modes for identification of the non-linear motions is also investigated by means of extensive simulations. Lower dimensional models are then created using these K–L modes to reconstruct the responses of the system and comparison to the actual responses is made. It should be noted that the K–L modes do not have physical significance other than the fact that they best approximate the spatial dependence of the dynamics. However, the K–L modes of a linear undamped and unforced system, undergoing normal mode oscillations, are identical to the physical modes of the system. The comparisons between the K–L modes and the physical modes are made in reference [19].

It was observed that the K–L method provides a measure of the non-linear effects of the system. This is consistently manifested as transfer of energy from low to high order K–L modes as the degree of the non-linearity is varied. This behavior was also typical in the experiments performed on a vibroimpacting rotor. The energy contained in the K–L modes can serve as a measure of the dimensionality of the system and can be used effectively in sub-structuring large-scale systems. The use of the K–L method to reconstruct the system dynamics using a lower order model has yielded satisfactory results and a reduction in computational time. This method can be applied in a cost-effective manner to practical engineering structures for online defect monitoring, especially, when acceleration fields are used in K–L decomposition. Moreover, the extremely small computational time is suited for online computation of modes and their changes.

Finally, it is noted that the above work presents a framework for applying the K–L method to continuous systems undergoing vibroimpacts. It presents the results of the numerical and experimental work done on vibroimpacting beams and rotors. The numerical schemes, numerical issues, experimental limitations and methods to overcome these have been mentioned here. For in-depth details the reader is referred to reference [17]. This work could add to the knowledge base of the application of K–L method to vibroimpacting systems and in the future the method can be generalized in the application to diagnosis and monitoring of defects, much in the way it is done for linear systems currently.

REFERENCES

1. V. R. Algazi, K. L. Brown and M. J. Reddy 1993 *IEEE Transactions on Speech and Audio Processing* **1**, 180–195. Transform representation of the spectra of acoustic speech segments with applications, Part I: general approach and application to speech recognition.
2. S. A. Zahorian and M. Rothenberg 1981 *Journal of the Acoustical Society of America* **69**, 519–524. Principal component analysis for low-redundancy encoding of speech spectra.
3. P. Holmes, J. L. Lumley and G. Berkooz 1996 *Turbulence, Coherent Structures. Dynamical Systems and Symmetry*. Cambridge, New York.
4. L. Sirovich, B. W. Knight and J. D. Rodriguez 1990 *Quarterly of Applied Mathematics* **XLVIII**, 535–548. Optimal low-dimensional dynamic approximation.
5. J. D. Rodriguez and L. Sirovich 1990 *Physica D* **43**, 77–86. Low dimensional dynamics for the complex-Landan equation.
6. M. Rajaee, S. K. F. Karlsson and L. Sirovich 1994 *Journal of Fluid Mechanics* **258**, 1–29. Low-dimensional description of free-shear-flow coherent structures and their dynamical behavior.
7. L. Sirovich and M. Kirby 1989 *Physics of Fluids* **A2**, 127–136. An eigenfunction approach to large scale transitional structures in jet flow.
8. K. Karhunen 1946 *Annals of Academic Science Fennicae Series A*1, *Mathematical Physics* **37**, Uber lineare methoden in der wahrscheinlichkeitsrechnung.
9. M. M. Loeve 1955 *Probability Theory*. Princeton NJ: Von Nostrand.
10. H. Tarman 1996 *International Journal for Numerical Methods in Fluids* **22**, 67–79. A Karhunen–Loeve analysis of turbulent thermal convection.
11. M. D. Graham and I. G. Kevrekedis 1996 *Computers and Chemical Engineering* **20**, 495–506. Alternative approaches to the Karhunen–Loeve decomposition for model reduction and data analysis.
12. L. Sirovich 1987 *Quarterly of Applied Mathematics* **45**, 561–571. Turbulence and the dynamics of coherent structures. Part I: coherent structures.
13. H. M. Park and D. H. Cho 1996 *Chemical Engineering Science* **51**, 81–98. The use of Karhunen–Loeve decomposition for the modeling of distributed parameter systems.
14. J. L. Mari and F. Glangeaud 1994 *Revue De L' Institut Francis Du Petrole* **49**, 21–75. Wave separation application.
15. J. P. Cusumano, M. T. Sharkady and B. W. Kimble 1994 *Philosophical Transactions of the Royal Society of London* **347**, 421–438. Dynamics of a flexible beam impact oscillator.

16. A. BENGUEDOUAR 1995 *Ph.D. Thesis, Boston University*. Proper orthogonal decomposition in dynamical modeling: a qualitative dynamic approach.
17. M. F. A. AZEEZ 1998 *Ph.D. Thesis, University of Illinois at Urbana-Champaign*. Theoretical and experimental studies of the nonlinear dynamics of a class of vibroimpact systems.
18. E. EMACI, T. A. NAYFEH and A. F. VAKAKIS 1997 *Zeitschrift fur Angewandte Mathematik und Mechanik* (*ZAMM*) **77**, 527–541. Numerical and experimental study of nonlinear localization in a flexible structure with vibro-impacts.
19. B. F. FEENY 1997 *Proceedings of the* 1997 *ASME Design Engineering Technical Conference. Sacramento, CA*. Interpreting proper orthogonal modes in vibrations.
20. K. OGATA 1997 *Modern Control Engineering*. Englewood Cliffs. NJ: Prentice-Hall; third edition.
21. B. A. FINLAYSON 1972 *The Method of Weighted Residuals and Variational Principles. Mathematics in Science and Engineering*, Vol. 87. New York: Academic Press.
22. IMSL, Inc, Houston, Texas 1991 *FORTRAN Subroutines for Mathematical Applications.*
23. M. F. A. AZEEZ and A. F. VAKAKIS 1999 *International Journal of Nonlinear Mechanics* **34**, 415–435. Numerical and experimental analysis of a continuous overhung rotor undergoing vibro-impacts.
24. M. F. A. AZEEZ and A. F. VAKAKIS 1997 *Proceedings of the ASME Design Engineering Technical Conference, Sacramento, CA*. Numerical and experimental analysis of the nonlinear dynamics due to impacts of a continuous overhung rotor.
25. I. T. GEORGIOU, I. SCHWARTZ, E. EMACI and A. F. VAKAKIS 1999 *Journal of Applied Mechanics* **66**, 361–367. Interactions between slow and fast oscillations in an infinite degree-of-freedom linear system coupled to a nonlinear subsystem: theory and experiment.